Cell Reports

Article

Spatial compartmentalization of signaling imparts source-specific functions on secreted factors

Graphical abstract

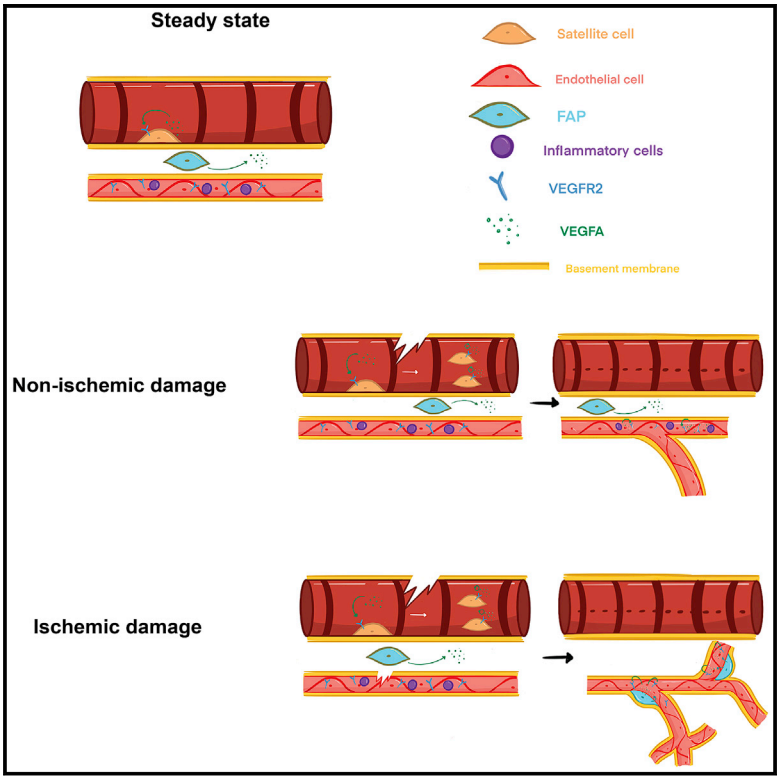

Authors

Elena Groppa, Paolo Martini, Nima Derakhshan, ..., Helen M. Blau, Chiara Romualdi, Fabio M.V. Rossi

Correspondence

fabio@brc.ubc.ca

In brief

Groppa et al. perform a time-resolved bioinformatics analysis that highlights extensive ligand-receptor redundancy among the cell types contributing to skeletal muscle regeneration. They focus on one of these pathways and show that VEGFA from different cell types has distinct roles in regeneration.

Highlights

- Ligand-receptor signaling redundancy during skeletal muscle regeneration
- Inflammatory cells and muscle and fibro/adipogenic progenitors produce VEGFA
- VEGFA from muscle progenitors controls their proliferation after muscle damage
- VEGFA from FAP controls angiogenesis only after ischemic damage

Groppa et al., 2023, Cell Reports *42*, 112051
February 28, 2023
https://doi.org/10.1016/j.celrep.2023.112051

CellPress

Cell Reports

CellPress
OPEN ACCESS

Article

Spatial compartmentalization of signaling imparts source-specific functions on secreted factors

Elena Groppa,[1,2] Paolo Martini,[3,4,9] Nima Derakhshan,[1,9] Marine Theret,[1] Morten Ritso,[1] Lin Wei Tung,[1] Yu Xin Wang,[5] Hesham Soliman,[1,6,7] Mark Stephen Hamer,[1] Laura Stankiewicz,[1] Christine Eisner,[1] Le Nevé Erwan,[8] Chihkai Chang,[1] Lin Yi,[1] Jack H. Yuan,[1] Sunny Kong,[1] Curtis Weng,[1] Josephine Adams,[1] Lucas Chang,[1] Anne Peng,[1] Helen M. Blau,[5] Chiara Romualdi,[4] and Fabio M.V. Rossi[1,10,*]

[1]School of Biomedical Engineering, University of British Columbia, 2222 Health Sciences Mall, Vancouver, BC, Canada
[2]Borea Therapeutics, Scuola Internazionale Superiore di Studi Avanzati, Via Bonomea 265, Trieste, Italy
[3]Department of Molecular and Translational Medicine, University of Brescia, Brescia, Italy
[4]Department of Biology, University of Padova, via U. Bassi 58B, Padova, Italy
[5]Baxter Laboratory for Stem Cell Biology, Department of Microbiology and Immunology, Stanford University School of Medicine, Stanford, CA, USA
[6]Faculty of Pharmaceutical Sciences, Minia University, Minia, Egypt
[7]Aspect Biosystems, 1781 W 75th Avenue, Vancouver, BC, Canada
[8]Department of Pediatrics, Université Laval, Laval, QC, Canada
[9]These authors contributed equally
[10]Lead contact
*Correspondence: fabio@brc.ubc.ca
https://doi.org/10.1016/j.celrep.2023.112051

SUMMARY

Efficient regeneration requires multiple cell types acting in coordination. To better understand the intercellular networks involved and how they change when regeneration fails, we profile the transcriptome of hematopoietic, stromal, myogenic, and endothelial cells over 14 days following acute muscle damage. We generate a time-resolved computational model of interactions and identify VEGFA-driven endothelial engagement as a key differentiating feature in models of successful and failed regeneration. In addition, the analysis highlights that the majority of secreted signals, including VEGFA, are simultaneously produced by multiple cell types. To test whether the cellular source of a factor determines its function, we delete VEGFA from two cell types residing in close proximity: stromal and myogenic progenitors. By comparing responses to different types of damage, we find that myogenic and stromal VEGFA have distinct functions in regeneration. This suggests that spatial compartmentalization of signaling plays a key role in intercellular communication networks.

INTRODUCTION

Regeneration and development are among the many biological processes that require highly dynamic changes in cellular functions to take place in a coordinated fashion across multiple cell types. Such multicellular synchronization occurs via intercellular interactions mediated by a variety of signals, including a diverse number of secreted factors and their cognate receptors. Disruption of these cellular networks is likely implicated in pathogenic responses to damage, such as fibrosis. Understanding the rules that govern intercellular communication and formulating predictive models capable of highlighting specific interactions have the potential to identify therapeutic intervention points.

To date, work toward the creation of such models has been mainly carried out in developmental systems. In RNA sequencing (RNA-seq) datasets, manual curation has been applied to define lists of relevant factors and receptors expressed by specific cell types. From these lists, interactions have been predicted computationally, generating models that represent ongoing interactions.[1–6] In all cases, these models were created using data gathered at a single time point and fail to capture the temporal dynamics of "cellular interactomes" as they exist *in vivo* over the course of a physiological response.

Skeletal muscle is a highly regenerative tissue capable of complete functional restoration following damage.[7] However, pathologies such as chronic damage (e.g., muscular dystrophies) and aging result in loss of this regenerative capacity, providing a clinically compelling reason to identify strategies for restoring it.[8,9] Here, we generated a dynamic model of skeletal muscle regeneration based on recurrent RNA-seq sampling of multiple purified cell populations involved in the regenerative response to acute damage. We focused on communication across (1) muscle stem cells, also called satellite cells; (2) tissue-resident mesenchymal fibro/adipogenic progenitors; (3) immune cells; (4) pericytes; and (5) endothelial cells. Previous studies have revealed a complex web of regulatory interactions among these cell types.[10–26] This intercellular communication landscape is highly dynamic, with the same cell lineages carrying out drastically

different and sometimes opposing functions at different times after damage.[27,28]

We built a bioinformatics pipeline and used it to assemble a time-resolved interactome that connects the different skeletal muscle cell populations through either autocrine or paracrine ligand-receptor interactions. To identify the cellular interactions responsible for regeneration, we employed this pipeline to compare the responses in wild-type mice with those of mice lacking C-C chemokine receptor 2 (CCR2 knockout [KO]),[20,24] a mouse strain in which circulating blood-derived monocytes are unable to infiltrate the parenchyma of damaged tissue, impairing muscle regeneration. We found that a key difference between the two models was the extent of engagement of endothelial cells, and we identified the lack of VEGFA from infiltrating macrophages as a causative factor.

Surprisingly, our analysis shows that VEGFA, as well as the vast majority of ligands and their cognate receptors, are expressed by multiple cell lineages within regenerating muscle. The pleiotropic activity of VEGFA signaling in a variety of cell types that are in close proximity, like endothelial and myogenic cells,[11] prompted us to use this signaling as a benchmark to question whether ligands from different lineages function equally and exist purely to provide redundancy and, therefore, robustness or whether the cell of origin of a given secreted factor imparts specificity on its role during the regenerative process. Previous studies have investigated the effect of VEGFA depletion in a specific compartment (for example, myogenic progenitors [MPs],[2,29] myofibers,[29,30] and inflammatory cells,[24,31]), but they did not explore whether the role of other VEGFA sources is functionally equivalent. To experimentally address this, we deleted the VEGFA gene individually in each of its sources (i.e., inflammatory cells, MPs, and fibro/adipogenic progenitors [FAPs]) and tested its activity in two types of injury models: ischemic and non-ischemic.

Our results support the notion that signaling is spatially compartmentalized *in vivo* and that the cellular origin of a ligand strongly impacts its function, with distinct cell lineages playing critical roles in response to specific types of damage. We conclude that inclusion of spatial information and anatomical features in cellular interaction models will be critical to understand the ground rules underlying intercellular signaling *in vivo*.

RESULTS

A time- and lineage-resolved transcriptional analysis of regeneration

To describe the intercellular communication network that supports skeletal muscle regeneration, we purified FAPs, endothelial cells (ECs), MPs, inflammatory cells (ICs), and pericytes (PERs) at steady state and at multiple time points after muscle damage. We induced damage by intramuscular injection of notexin (NTX), a myotoxin, in the *tibialis anterior* (TA) muscle in wild-type (WT) and CCR2KO mice, which provided models for efficient and delayed regeneration, respectively. In addition to purified populations from each genotype, whole TA bulk tissue samples from WT mice were also collected and analyzed at each time point. We subjected all samples to RNA-seq and assembled a multistep bioinformatics analysis workflow, part of which is schematically represented in Figure S1A. We first identified differentially expressed genes (DEGs) in each cell subset (cell-type-specific analysis), followed by genes whose change in overall abundance is associated with expansion of specific cell subsets rather than with changes in their transcriptional output per cell, and finally genes that are constitutively expressed by specific cell subsets. Next, based on the selected genes, we inferred cross-talk among specific cell subsets by pairing expression of ligands (Ligs) and their cognate receptors (Recs). Finally, we determined the biological processes associated with DEGs and Lig-Rec pairs in each cell type.

Principal-component analysis (PCA) on FAPs, ECs, MPs, ICs, and PERs transcriptomes pooled from all collected time points displayed clear separation among the cell subsets, confirming their distinct nature and lack of ambiguity in their definition (Figures S1B and S1C). Next, we assessed transcriptome dynamics in each cell type during muscle regeneration by comparing gene expression across the different collection time points. We employed two types of bioinformatics analyses, silhouette and biological homogeneity index, to generate clusters grouping the different time points in a time-unbiased manner and estimate similarity across clusters. Samples clustering together across multiple time points in the PCA plots (Figures 1B and 1C, clusters are color coded) indicate that the transcriptome, and presumably the function, of that specific cell type did not significantly change over time. Samples in which each cluster contains all samples from a subset of time points (Figures 1A and 1D) suggest that, over time, cells moved through a discrete set of transcriptional states, likely indicating different functions. When performed on whole-tissue samples, this analysis clearly showed that the regenerative process relies on well-defined, temporally distinct stages (Figure S1D). Next, we investigated which of the tissue-resident lineages are most dynamic and therefore most likely to drive transitions across the different phases of regeneration. We initially focused on FAPs, which showed highly dynamic behavior, and ECs, which changed very little over the time course (Figures 1A and 1C). FAP transcriptomes were grouped in four clusters based on silhouette analysis, suggesting that they move through four main states during the repair process, with each of the clusters containing all replicates of the same time points, as shown by the high level of homogeneity index (0.6). Specifically, we found that FAPs transitioned through two distinct stages early after damage (the day 1 and day 2 time points formed two discrete clusters), followed by a third state (spanning days 3, 4, 5, and 6), and finally entered into fourth steady state shared by the undamaged and late time points (days 0, 7, 10, and 14), as recently described by others.[32] This ordered progression was disrupted in CCR2KO mice, in which clusters displayed a much lower homogeneity index (0.35), suggesting a key role of infiltrating ICs in temporal organization of FAP transition states and the overall regenerative process (Figures 1A and 1B). This is consistent with our previous description of the behavior of FAPs in WT versus CCR2KO animals.[18]

Lack of IC-derived VEGFA is responsible for disrupted regeneration in CCR2KO mice

In contrast, EC clusters were characterized by a poor homogeneity index (0.21 with silhouette n = 4) in WT animals, which increased (0.7 with silhouette n = 3) in CCR2KO mice

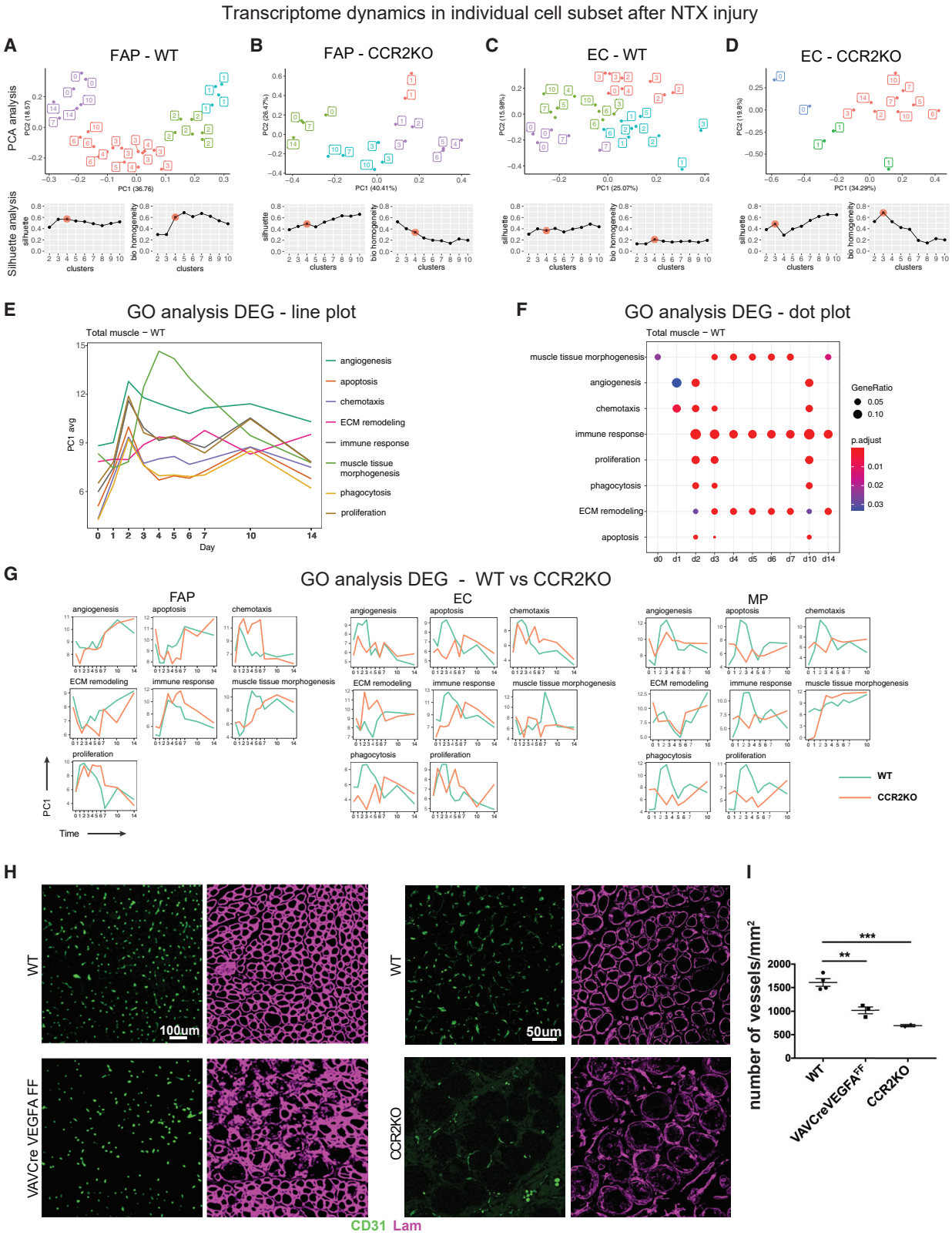

(legend on next page)

(Figures 1C and 1D). This suggests that NTX damage has only minor effects on the endothelium in WT mice but that the lack of infiltrating ICs in CCR2KO mice exacerbates the damage, leading to increased involvement of the endothelium during the regenerative process. Histological analysis confirmed that only limited vascular remodeling, observed as a small increase in vascular density immediately following NTX damage, was taking place in WT animals (Figures S1E and S1G). In CCR2KO mice, however, vessel disruption was much more evident, and the response appeared to be biphasic, with the vessels' diameter abnormally increasing early after damage, normalizing, and then increasing again 7 days post damage (Figures S1F and S1G). Increased vascular permeability, which was only observed on day 3 in controls, persisted until day 10 in CCR2KO mice (Figure S1H), consistently with the poor coverage by pericytes that regulate vascular integrity (Figure S1I).

To understand the biological activities associated with each cell lineage during normal and impaired muscle regeneration, we performed gene ontology (GO) biological process (BP) enrichment analysis based on DEGs from whole tissue and individual cell populations. With the goal of broadening as well as simplifying the outcomes of our analysis, we grouped GO BP terms into 8 main categories: muscle tissue morphogenesis, extracellular matrix (ECM) remodeling, immune response, apoptosis, chemotaxis, phagocytosis, proliferation, and angiogenesis. The results of our GO analysis were displayed as line plots, based on the top genes associated with PCA1, and dot plots, determined by the number of genes expressed by a cell type of the total genes attributed to a given GO metaclass (defined in STAR Methods and Table S1). In the whole tissue, apoptosis, chemotaxis, phagocytosis, proliferation, and angiogenesis were predominant at early stages of regeneration (day 1 to day 3 post injury), while immune response, muscle tissue morphogenesis, and ECM remodeling were first observed 2–3 days after damage and remained active throughout the later stages of the repair process, with muscle tissue morphogenesis gradually returning toward baseline by the endpoint (Figures 1E and 1F).

GO enrichment analysis on DEGs showed that all cell types participate in the biological processes observed in whole muscle, differing from each other mainly in the timing and extent of their contribution (Figures S2A and S2B). Further analysis revealed that many biological processes, like apoptosis and muscle tissue morphogenesis, were delayed in CCR2KO FAPs compared with WT FAPs (Figure 1G). In contrast, proliferation and chemotaxis were prolonged, in line with the phenotype described previously in CCR2KO FAPs.[18] Similarly, we found that angiogenesis, chemotaxis, and proliferation were delayed in ECs from CCR2KO compared with ECs from the WT, consistent with the abnormal vascular remodeling observed in CCR2KO versus WT mice after NTX damage (Figures 1G and S1E–S1I). Overall, WT MPs were more active than CCR2KO MPs, consistent with the impairment of the regenerative process in CCR2KO mice.

We tested the validity of the conclusions emerging from our GO enrichment analysis with additional bioinformatics and experimental investigations focused on cell proliferation. We determined the mitotic index (MI) from FAPs, ECs, and MPs in WT and CCR2KO mice.[33] In parallel, we measured EdU incorporation in FAPs, ECs, and MPs at different time points after NTX injection. A notable concordance was observed between proliferation kinetics extracted from GO data and MI as well as EdU experimental data (Figure S2C). While FAPs, ECs, and MPs in WT and CCR2KO mice proliferate from day 1 to day 3 post injury (early phase), they slowed drastically in WT mice after that point but continued to expand in CCR2KO animals.

A key molecule produced by infiltrating macrophages is VEGFA, a well-known pro-angiogenic factor whose absence from CCR2KO mice might impair the endothelial response to damage. To test whether this was the case, we deleted VEGFA from all hematopoietic lineages by generating VAVCre VEGFA^{FF} mice (~95%; data not shown). In these animals, we found a reduction of vessel density consistent with the impaired vascular remodeling observed previously in our CCR2KO model, where recruitment of VEGFA-producing monocytes from the bloodstream is absent (Figures 1H and 1I). This also resulted in disrupted muscle regeneration to a degree similar to that observed in CCR2KO mice, confirming that hematopoietic VEGFA was indeed a critical missing signal when inflammatory infiltration was prevented. In accordance with our previous work, we did not observe the typical fibrofatty infiltration triggered by damage in the absence of IC recruitment, which is caused by lack of tumor necrosis factor-α (TNF-α)[18] (Figure S2D).

In conclusion, our time-resolved transcriptomics analysis is capable of measuring the extent to which specific cell types are recruited by and contribute to regeneration. In addition, it pinpoints disruptions of the cells' normal progress through distinct phases of the regenerative process. Together, this allowed deconvolution of the complex phenotype of CCR2KO mice and identification of a functionally relevant biological process perturbed in this model.

Intercellular communication networks are promiscuous

Most developmental processes, including adult tissue regeneration, are supported by a rich network of intercellular communications.

Figure 1. Distinct cellular activation in normal and delayed regeneration

(A–D) Silhouette, biological homogeneity index, and PCA for FAP and EC RNA-seq data collected throughout the response to myotoxin damage from WT and CCR2KO mice. In the PCA plots, the number in each box represents the time of harvest in days post damage, with zero representing undamaged samples. The color of the box indicates which samples cluster together. The representative values described in the main text are highlighted with red filled circles.

(E) Representation of the 8 main Gene Ontology (GO) categories over time in whole WT muscle.

(F) GO enrichment analysis for the 8 main categories; dot color reflects adjusted p value and dot size the ratio between category-associated DEGs and total number of genes in the category.

(G) Comparison of expression over time in each indicated cell type (FAP, EC, and MP) of the genes associated with the 8 GO categories in WT and CCR2KO mice.

(H) Representative image of muscles collected from WT, VAVCre VEGFA^{FF}, and CCR2KO mice 7 days after NTX damage (scale bar, 50–100 μm).

(I) Quantification of vessel density based on CD31 staining of WT, VAVCre VEGFA^{FF}, and CCR2KO mice 7 days after NTX damage (n = 3–4, data represent the mean ± SEM, one-way ANOVA with multiple comparisons, $^{**}p < 0.01$, $^{***}p < 0.001$).

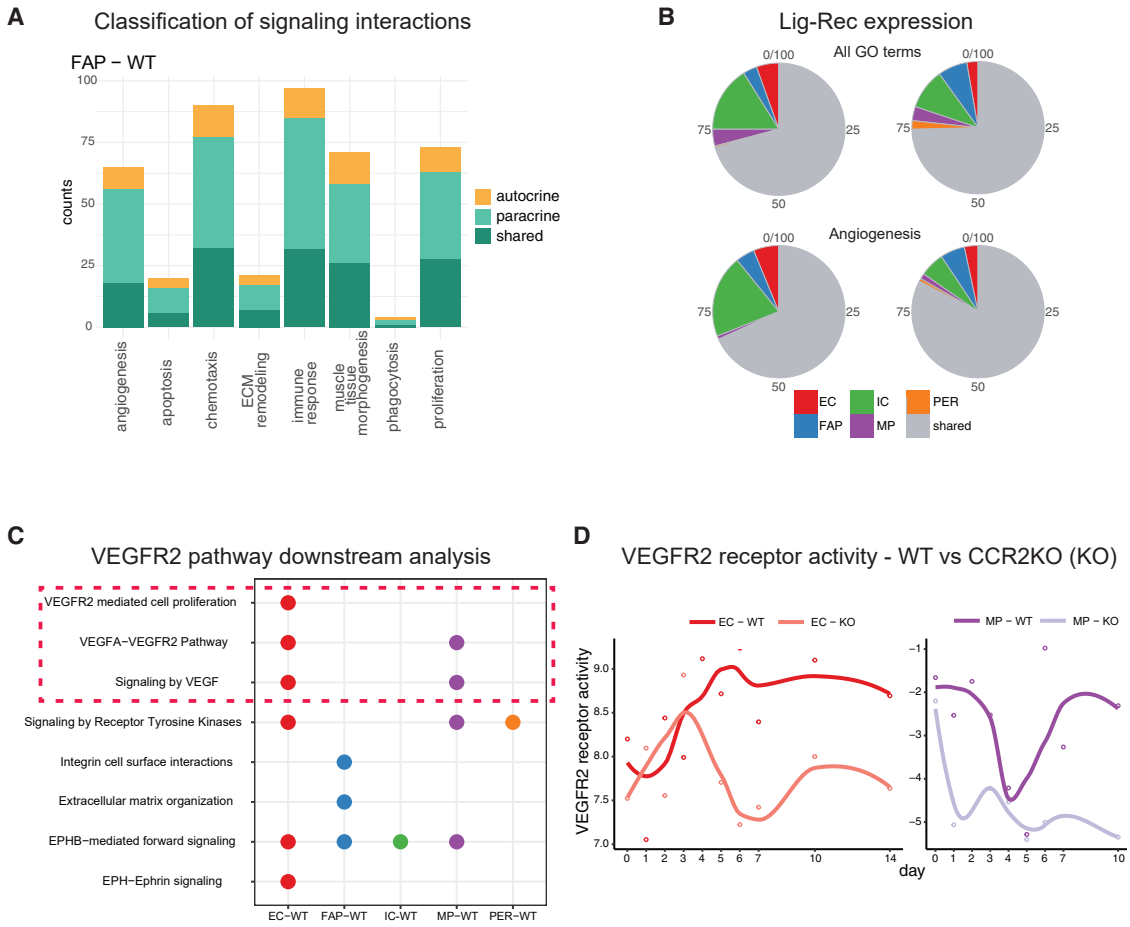

Figure 2. VEGFA, an example of promiscuous intercellular communication

(A) Classification of signaling interactions of FAPs by GO category. Interactions are classified as autocrine when FAPs express cognate ligand and receptor (yellow), paracrine when FAPs expresses one but not the other (light green), and "shared" when FAPs engage in autocrine or paracrine signaling but the ligand or receptor is also expressed by other cells (dark green).

(B) Pie charts show the percentage of ligands and receptors expressed by only one cell type (colors) or shared by more than two cell types (gray).

(C) VEGFR2-related pathway activation in different cell types (TimeClip analysis).

(D) Activation profile (Viper analysis) of *Kdr* (VEGFR2) in ECs and MPs from WT and CCRKO mice at different time points after NTX damage.

With the goal to begin describing such networks in the context of muscle regeneration, we built a time-resolved map of autocrine and paracrine signaling based on pairing manually curated lists of expressed receptors and ligands and analyzed it through GO pathway enrichment. For each cell type and GO category analyzed, we subdivided the type of interaction as autocrine when the same cell type expressed cognate ligand and receptor, paracrine when a cell type expressed one but not the other, and "shared" when a cell type engaged in autocrine or paracrine signaling but the ligand or was also expressed by other cell types. We found each category to be represented in each GO and cell type, with shared interactions representing a surprisingly large proportion of the cellular interactome (Figures 2A and S3A). This suggests that each cell type interacts with multiple other cell populations through the same Lig-Rec interactions. In line with this finding, we observed that nearly 75% of all receptors and ligands are expressed at the same time by two or more cell types (Figure 2B).

In summary, we found that, during regeneration, the vast majority of ligands have multiple cellular sources and cellular targets. This could represent true redundancy, in which ligands produced by different cells carry out the same function in the context of regenerating tissue and multiple sources serve to confer robustness to the system. Alternatively, the same ligands could modulate specific tasks depending on their cell of origin.

VEGFA from MPs, but not from FAPs, is important in skeletal muscle regeneration after acute damage

To assess whether ligands originating from different cell types are functionally equivalent, we again focused on VEGFA signaling because it is vital for successful regeneration. Interestingly, beyond modulating angiogenesis, VEGFA has been proposed to have additional functions in healthy and diseased muscle.[2,34] In undamaged and damaged muscles, the ligand *Vegfa* can be produced by FAPs, MPs, and ICs (Figure S3B; Table S2). While its main receptor *Kdr* (VEGFR2) is restricted to

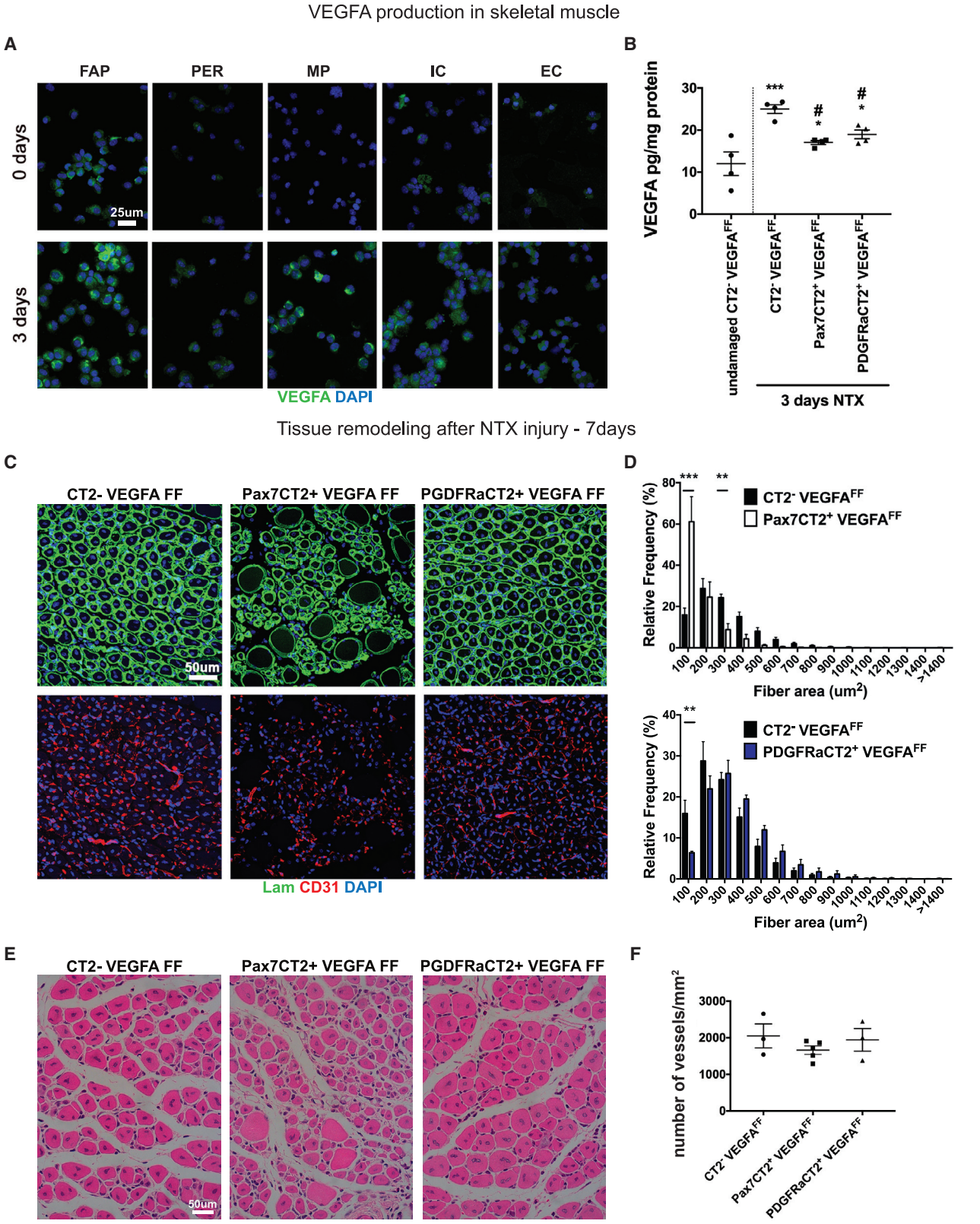

(legend on next page)

MPs and ECs, co-receptors like *Nrp1*, *Nrp2*, and *EphB2* are also expressed by more than one cell type.

We first verified that the pathway is indeed functional during regeneration by applying two computational approaches: (1) regulatory network analysis (Viper analysis), which determines the activity of a protein based on the number of co-expressed genes that belong to the same network unit, and (2) functional validation of receptor activity (TimeClip[35]), which elucidates activation of receptor downstream signaling over time. Based on the first analysis, we confirmed the activation of gold-standard receptors for the different cell populations, such as PDGFRa for FAPs, PDGFRb for PERs, CCR2 for ICs, Tek for ECs, and Notch3 for MPs (Figure S4A). As expected, VEGFR2 was strongly active in ECs but to a lesser extent also activated in ICs, MPs, and PERs. In the second approach, we integrated these results with the analysis of signaling downstream of VEGFR2 over time, which showed that VEGFA/VEGFR2 signaling is specifically active in ECs and MPs but not in other cell subsets, consistent with the outputs of the intercellular network (Figure 2C). Interestingly, a regulatory network analysis on ECs and MPs derived from WT and CCR2KO mice showed reduced and delayed VEGFR2 activity in CCR2KO mice (Figure 2D).

The effects of VEGFA depletion from ICs have already been reported in regenerative processes such as skin wound healing,[24] but less is known about the role of VEGFA produced by MPs and FAPs during muscle regeneration. First, we stained for VEGFA protein on cells sorted from muscle immediately following acute damage. As predicted in our bioinformatics analysis, and consistent with recently published results,[2] we confirmed that it is produced by multiple cell types, including significant contributions from FAPs and MPs (Figure 3A). We next assessed the specific contribution of MPs and FAPs to overall VEGFA levels in the tissue by depleting it in different cell subsets. To this end, we generated two mouse strains in which both alleles of VEGFA are floxed. The first strain carries the FAP-specific PDGFRα CT2$^+$ (FAP^{VEGFAKO}), while the second contains the MP-specific Pax7 CT2$^+$ (MP^{VEGFAKO}). After inducing Cre activation by tamoxifen treatment, we damaged the muscles with NTX and collected the tissues 3, 7, and 10 days after injury. The efficiency of VEGFA deletion was similar (~85%; data not shown) in both Cre systems. ELISA for VEGFA on whole tissue revealed that its depletion in either MPs or FAPs reduced the total amount of this factor by a comparable amount, providing quantitative support that their contribution to VEGFA secretion is similar during muscle regeneration after NTX damage (Figure 3B). IC infiltration, comparable quantitively and in terms of cell phenotypes across the three systems, was observed 3 days after damage (Figure S4B). 7 days post injury, we observed no difference in gross muscle organization in FAP^{VEGFAKO} compared with control CT2$^-$ VEGFA floxed (WT) mice, but found that the newly forming fibers were smaller and displayed disorganized morphology in tissues derived from MP^{VEGFAKO} mice (Figures 3C–3E). Scattered around these fibers, enlarged swollen myofibers were visible in MP^{VEGFAKO} muscles, a sign of impaired regeneration. Because these myofiber were not centrally nucleated (i.e., in regeneration), they were not integrated in the analysis of the cross-sectional area (CSA). Interestingly, there was no difference in vasculature density among the three groups (Figure 3F). Ten days after NTX, WT and FAP^{VEGFAKO} mice showed normal muscle regeneration, represented by fibers with homogeneous diameter size, while MP^{VEGFAKO} was still characterized by smaller muscle fibers (Figure S4B).

These data suggest that, while VEGFA from MPs is critical for efficient skeletal muscle repair following acute myotoxin damage, VEGFA from FAPs is not only dispensable but fails to rescue the phenotype resulting from ablation of VEGFA in MPs. Thus, autocrine VEGFA produced by MPs acts through a signaling network that paracrine VEGFA from FAPs is unable to activate despite the close proximity of the two cell types in the tissue. Additionally, neither MP- nor FAP-derived VEGFA has an effect on regenerative angiogenesis in this setting.

VEGFA controls MP proliferation but not differentiation

To investigate the mechanism underlying the observed phenotype, we measured MP proliferation 3 and 7 days post injury in mice that received a single EdU dose the day before harvest. 3 days post injury, MPs from MP^{VEGFAKO} mice were less proliferative and less abundant than in control animals, but overall TA muscle mass was comparable (Figure 4A). 7 days post injury, the observation had completely reversed; a higher percentage of MPs was proliferating in MP^{VEGFAKO} mice than in control mice, and this compensatory expansion led to normalization of the number of MPs (Figure 4B). However, TA muscle mass was reduced in MP^{VEGFAKO} animals. Consistent with the lack of vessel density impairment in MP^{VEGFAKO} mice, we did not see any difference in EC proliferation (Figure S5A). Similar assays performed with MPs isolated from FAP^{VEGFAKO} mice showed that VEGFA depletion in FAPs does not reduce either MP or EC proliferation and is consistent with the lack of phenotype observed in muscles of FAP^{VEGFAKO} mice.

To better understand how deletion of VEGFA in MPs affects muscle regeneration, we analyzed MP activation and differentiation by performing Pax7, Ki67, MyoD, and myogenin staining 3 and 7 days post injury. As expected from the previous results, MP^{VEGFAKO} mice displayed lower MP activation, shown by a decrease in the number of Ki67$^+$/Pax7$^+$ and MyoD$^+$ cells 3 days after damage (Figures 4C, 4D, 4G, and S5B), which led to a dramatic decrease in the number of myogenin$^+$ cells

Figure 3. VEGFA from MPs, but not from FAPs, is important in skeletal muscle regeneration after acute damage

(A) VEGFA staining on cytospin of FAPs, ECs, MPs, ICs, and PERs purified from skeletal muscle before and after acute damage (scale bar, 25 μm).

(B) Whole skeletal muscle VEGFA ELISA (n = 4, data represent the mean ± SEM, one-way ANOVA with multiple comparisons; *p < 0.05, ***p < 0.001).

(C) Skeletal muscles collected from WT, MP^{VEGFAKO}, and FAP^{VEGFAKO} 7 days after NTX damage and stained with laminin and CD31 (scale bar, 50 μm).

(D) Quantification of fiber size of the samples shown in (C); n = 3–4, data represent the mean ± SEM, two-way ANOVA with multiple comparisons; **p < 0.01, ***p < 0.001.

(E) H&E staining of skeletal muscles collected from WT, MP^{VEGFAKO}, and FAP^{VEGFAKO} mice 7 days after NTX (scale bar, 50 μm).

(F) Quantification of vessel density of the samples shown in (C); n = 3–5, data represent the mean ± SEM, one-way ANOVA with multiple comparisons.

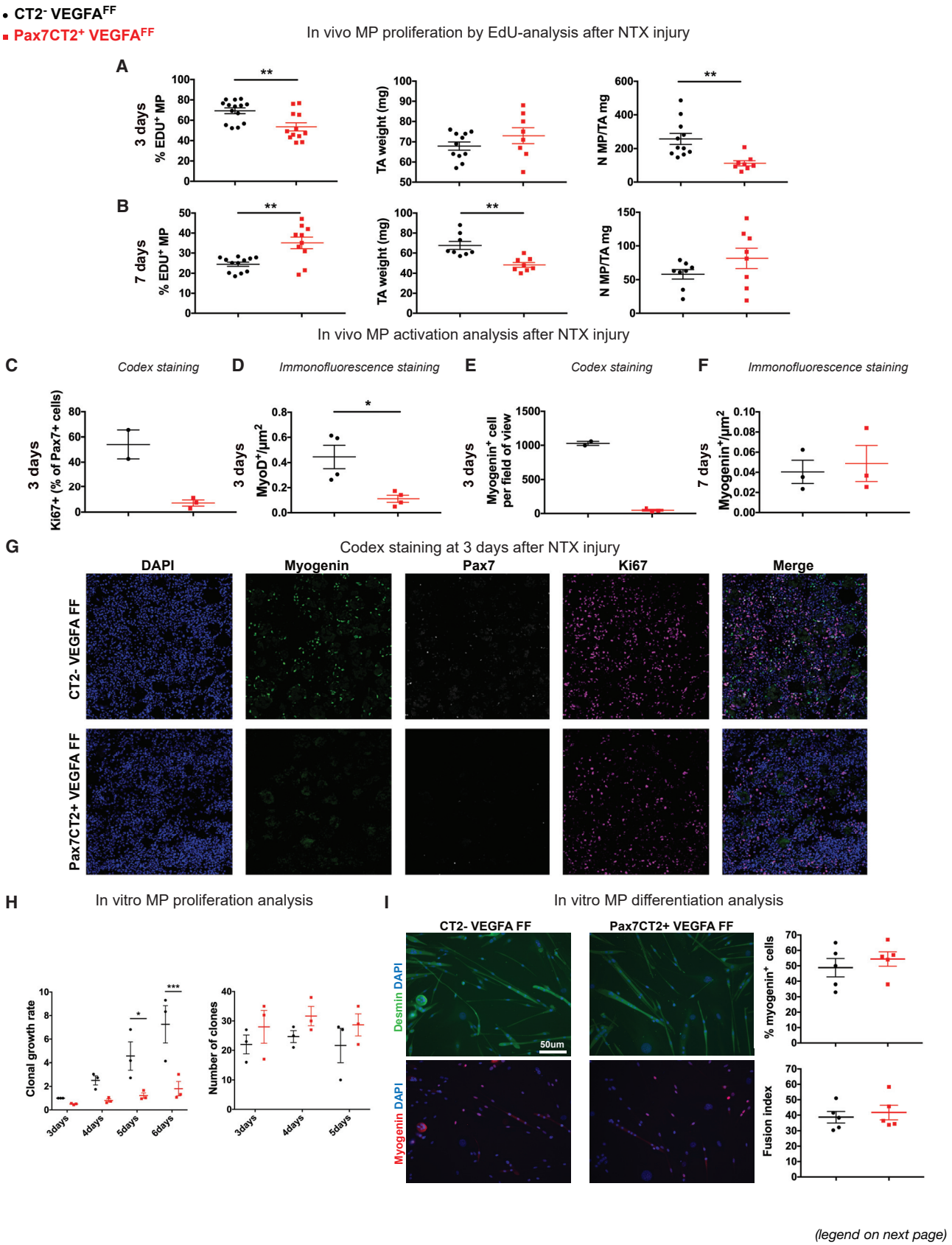

(legend on next page)

(Figures 4E and 4G). However, consistent with the MP proliferation recovery in $MP^{VEGFAKO}$ mice, we did not notice any difference in the number of myogenin$^+$ cells between $MP^{VEGFAKO}$ and WT mice 7 days after injury (Figures 4F and S5C).

Recent studies have also described the role of VEGFA in supporting MP survival;[34] thus, we analyzed apoptosis in our systems and noticed an increase in the number of MyoD$^+$/Tunel$^+$ MPs in $MP^{VEGFAKO}$ compared with WT animals (Figure S5D). This suggests that the reduction of the number of differentiating MPs 3 days after injury might be due to either impairment of proliferation or increase of apoptosis caused by VEGFA depletion specifically in MPs or both.

The reduced MP proliferation in $MP^{VEGFAKO}$ mice suggests that VEGFA may act through an autocrine loop in these cells. Indeed, MPs express the VEGFA receptors *Kdr* (VEGFR2), *Flt1* (VEGFR1), and *Nrp1* (Neuropilin-1) (Figure S5E). To confirm this hypothesis, we isolated MPs from $MP^{VEGFAKO}$ mice and compared their bulk and clonal expansion as well as their myogenic differentiation with control cells. Impairment of MP proliferation was readily observed in bulk cultures 7 days after cell seeding (Figure S5F). Clonal assays confirmed that VEGFA-depleted MPs were less capable of expansion than control cells but displayed similar colony formation efficiency (Figure 4H). This suggests that, *in vitro*, the lack of VEGFA does not impair survival of quiescent MPs. When cells from $MP^{VEGFAKO}$ and control mice were induced to differentiate, we observed no differences in either their myogenin expression (a measure of commitment to differentiation) or their ability to fuse into multinucleated fibers (Figure 4I), as indicated by the normal numbers of differentiating myogenin$^+$ cells counted 7 days after NTX (Figure 4F). Thus, autocrine VEGFA acts directly on MPs by regulating their proliferative capacity early during regeneration.

FAP-derived VEGFA is critical after ischemic damage

Our results suggest that FAP-derived VEGFA is dispensable in the regenerative response to myotoxin damage. However, we showed FAPs to be a robust source of VEGFA *in vivo*. Based on their proximity to vasculature and a recent report of a role of FAPs in ensuring vascular integrity following ischemic damage,[36] we switched to a femoral artery ligation (Fem Lig) model. Compared with NTX damage, this model is characterized by increased muscle fiber damage, vascular branching, endothelial proliferation, and activation of hypoxia-related pathways, including the VEGFA signaling network (Figures S6A–S6F).

Compared with WT controls 14 days post injury, $FAP^{VEGFAKO}$ displayed reduced adipose tissue formation and increased necrosis, while adipose tissue deposition increased with negligible necrosis in $MP^{VEGFAKO}$ mice (Figures 5A–5F). Fiber size in WT and $MP^{VEGFAKO}$ mice was quantified and revealed no significant difference (Figure 5G). Interestingly, and in line with the NTX damage model 7 days after injury (Figure 3D), fibers in the $FAP^{VEGFAKO}$ model were larger than in control animals (Figures 5G and S7A). This divergent muscle repair across the three systems was observed already 5 and 7 days after Fem Lig (Figure S7B). In summary, FAP-derived VEGFA plays a much more important role in muscle repair following ischemic compared with myotoxin damage, while the effects of MP-derived VEGFA are similar in the two models.

Because ischemic damage results in extensive vascular remodeling, we focused on the effects of MP or FAP VEGFA depletion on ECs. Similar to what was observed following NTX injury, EC proliferation was not affected in $MP^{VEGFAKO}$ mice after ischemic damage (Figure 6A). Conversely, VEGFA depletion from FAPs significantly impaired EC proliferation 4 days after surgery and led to the appearance of large decellularized areas of muscle with sparse vasculature (Figures 6A–6F).

To test whether the vasculature was efficiently perfused, we intravenously injected fluorescent lectin, which labels ECs. Seven days after ligation surgery, the extent of labeling of CD31$^+$ cells was assessed, revealing a strong damage-induced reduction in lectin labeling after ischemic damage but no significant difference between $FAP^{VEGFAKO}$ and WT mice (Figure S7C).

Next, we asked whether the same MP delayed-proliferation phenotype that was evident in myotoxin-damaged $MP^{VEGFAKO}$ animals was also present after ischemic damage. Indeed, MP proliferation and total numbers were lower in $MP^{VEGFAKO}$ versus WT mice 2 days after ischemic damage (Figure 7A). As with myotoxin damage, at later time points, differences in MP proliferation were no longer detectable, and the difference in total MP numbers, while still present, was significantly reduced. Thus, the phenotype in $MP^{VEGFAKO}$ mice is the same, independent of the type of damage.

In contrast, FAP proliferation relative to WT control muscle was unchanged in $FAP^{VEGFAKO}$ mice at all time points, suggesting that FAPs are not engaged in autocrine proliferative signaling through this factor (data not shown). However, we observed an

Figure 4. Autocrine VEGFA controls early MP proliferation

(A and B) Left: EdU incorporation in MPs from WT and $MP^{VEGFAKO}$ mice 3 and 7 days after NTX injury and 24 h after EdU treatment. Center: TA muscle weight. Right: absolute number of MPs/mg of muscle in the same samples (n = 8–14, data represent the mean ± SEM, unpaired t test or Mann-Whitney test, $^{**}p < 0.01$).

(C–E) Quantification of Ki67/Pax7$^+$, MyoD$^+$, and myogenin$^+$ cells from skeletal muscle collected 3 days after NTX from WT and $MP^{VEGFAKO}$ animals; n = 2–4, data represent the mean ± SEM, unpaired t test, $^*p < 0.05$.

(F) Quantification of myogenin$^+$ cells from skeletal muscle collected 7 days after NTX from WT and $MP^{VEGFAKO}$ animals; n = 3, data represent the mean ± SEM, unpaired t test.

(G) Representative images of multiplexed immunofluorescence co-detection (CODEX) panel from skeletal muscle collected 3 days after NTX from WT and $MP^{VEGFAKO}$ animals.

(H) MPs sorted from uninjured skeletal muscles of WT and $MP^{VEGFAKO}$ mice were seeded at clonal density. Left: average number of cells forming one colony at different time points after cell seeding, normalized to the WT 3-day average. Right: absolute number of colonies (n = 3, data represent the mean ± SEM, two-way ANOVA with multiple comparison; $^*p < 0.05$, $^{***}p < 0.001$).

(I) Representative pictures of myogenic differentiation in WT and $MP^{VEGFAKO}$ cultures. Top: frequency of myogenin$^+$ cells (n = 5, data represent the mean ± SEM, unpaired t test). Bottom: fusion index (percentage of nuclei within syncytial structures) (n = 5, data represent the mean ± SEM, unpaired t test). Scale bar, 50 μm.

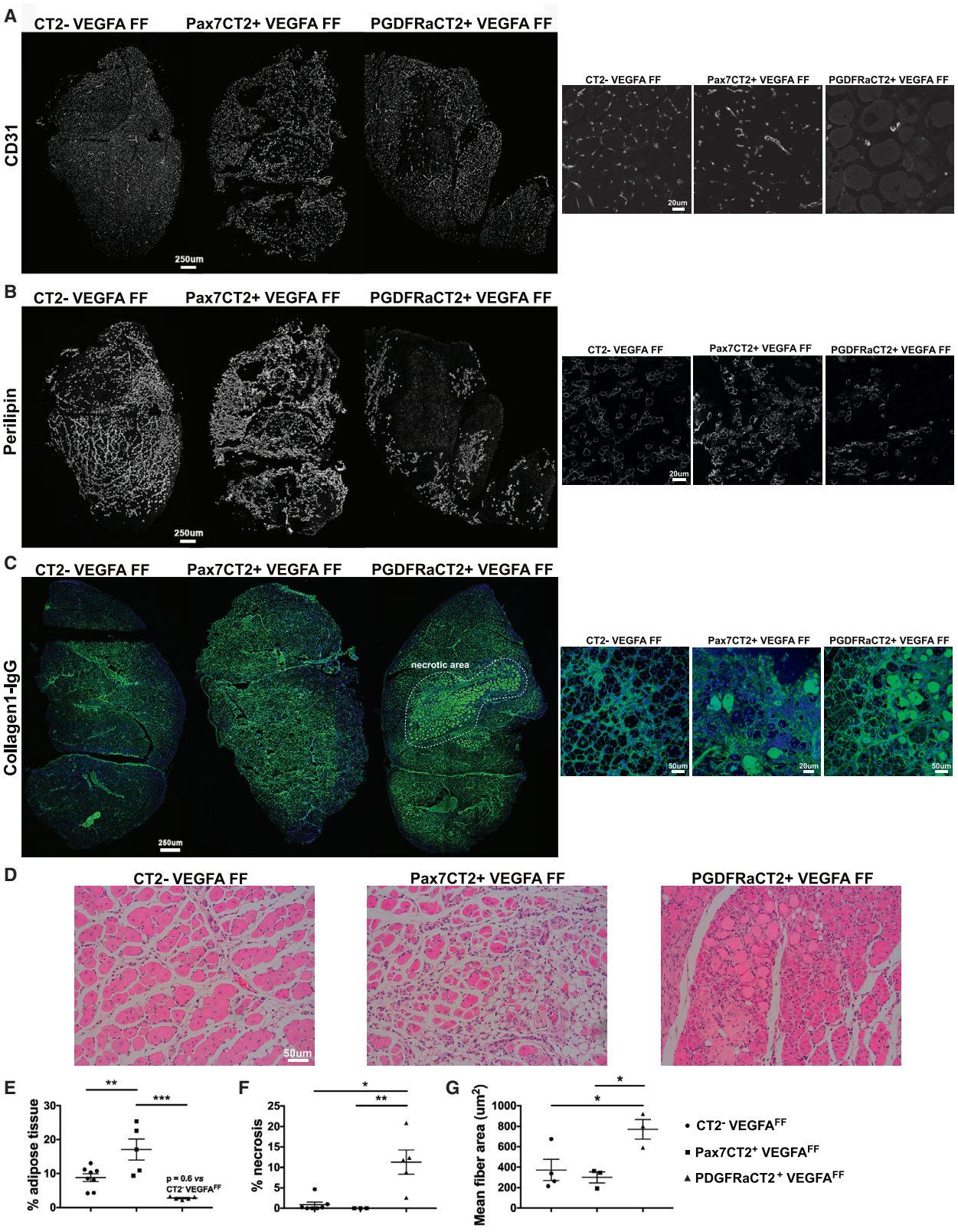

(legend on next page)

increase in adipocyte formation in TA muscle from $MP^{VEGFAKO}$ mice and a decrease in $FAP^{VEGFAKO}$ animals. These differences were already evident 5 days (Figures 7B and 7C) and still present 14 days after surgery (Figures 5B and 5E). We asked whether a lack of VEGFA in FAPs may modulate their ability to differentiate. FAPs from WT and $FAP^{VEGFAKO}$ were cultured and their proliferation and adipogenic potential compared. Consistent with the fact that FAPs do not express VEGFA receptors (Figure S5E), no difference was detected (Figures S7D and 7D).

To identify possible signaling events leading to impaired adipogenesis, we performed RNA-seq on FAPs and ECs sorted from TA muscle of WT and $FAP^{VEGFAKO}$ mice collected after Fem Lig. While we did not notice any major difference in FAPs derived from $FAP^{VEGFAKO}$ and WT mice, we noticed an upregulation of pro-inflammatory cytokines in ECs derived from $FAP^{VEGFAKO}$ mice versus their control (data not shown). One of these upregulated factors was interleukin-6 (IL-6), which has been described to impair adipogenesis.[37,38] Therefore, the upregulation of IL-6 found in ECs derived from $FAP^{VEGFAKO}$ mice could explain the reduction of adipogenesis observed in $FAP^{VEGFAKO}$ compared with control mice. Interestingly, IL-6 is also known to promote skeletal muscle hypertrophy,[39] which could explain the fiber hypertrophy observed in $FAP^{VEGFAKO}$ mice. Certainly, IL-6 is just one of the many candidates that could lead to the intriguing phenotype observed with $FAP^{VEGFAKO}$ mice in regard to adipogenesis and fiber hypertrophy, which we did not further characterize because this was not the central theme of our work.

The basement membrane compartmentalizes skeletal muscle and controls intercellular networks

Based on our data, the ability of VEGFA to reach a nearby target cell appears to be limited by factors other than physical distance or the inherent ability of the target cell to respond to it. We hypothesized that these observations might be due to the presence of physical barriers that limit intercellular cross-talk by confining VEGFA availability. Interestingly, we found that MPs and FAPs primarily express $VEGFA_{164}$, an isoform with a high affinity for ECM, and its precursor L-VEGFA (Figure 7E).[40]

Thus, we focused our attention on the main ECM-rich structural barrier in skeletal muscle, the basement membrane (BM). At steady state, we found a hierarchy of compartmentalization with FAPs separated from ECs and MPs by a single layer of BM, while ECs were separated from MPs by two layers (Figure 7F). In myotoxin and ischemic damage, the integrity of the barrier between MPs and ECs was maintained, and MPs remained confined within the BM of the muscle fiber. Similarly, following NTX injury, the positioning of ECs and FAPs relative to each other and the BM was left unperturbed, in agreement with the poor BM traversal by FAP described using spatial multiplexed imaging.[41] In contrast, ischemic damage led to remodeling of the BM, resulting in ECs and FAPs being embedded in the same BM layer. Such a change would allow VEGFA from FAPs to be delivered directly to the endothelial BM, while VEGFA from MPs would adsorb to the BM ensheathing the myofiber and be prevented from reaching ECs.

While physical barriers like the BM might constrain specific ECM-bound ligands, like some VEGFA isoforms, they should not limit the freely diffusible ones. We investigated this by focusing on another paracrine signal between FAP-produced Angiopoietin-1 (Angpt1), which lacks a matrix binding domain, and its receptor Tie2 (*Tek*), which is expressed by MPs and ECs (Figure S3B; Table S2). We depleted Angpt1 in perivascular cells using a previously published Cre-inducible system[28] and treated the mice with EdU for 3 weeks upon Angpt1 silencing. Interestingly, we observed increased MP proliferation in mice whose FAPs lacked Angpt1 versus WT animals, consistent with the known role of Angpt1/Tek in regulating MP quiescence (Figure 7G).[42] This indicates that the ECM represents a physical barrier for intercellular signaling occurring through ECM ligands, like VEGFA isoforms, but not diffusible ligand, like Angpt1.

In summary, we have shown that, despite the apparent high redundancy suggested by analyzing the expression of ligands and receptors, at least some signaling pathways are compartmentalized in adult tissues, and we propose that ECM-based structural barriers may play a role in determining who can signal to whom. Further work will be required to determine how widely this principle applies.

DISCUSSION

The robustness of tissue regeneration depends on a web of interactions between different cells. Within this network, dysregulation or loss of function in just one of these cell types can lead to functional disruption of multiple other cell types, making it difficult to assign the observed phenotype to a specific molecular pathway. Macrophages in muscle regeneration are an excellent example because they concomitantly signal to the endothelium, stroma, and myogenic cells.[10,18–20,23,24,43] Lack of infiltration by macrophages leads to regeneration failure, as observed in CCR2KO mice, but deconvolving the contribution of each of the target cell types to the overall phenotype and identifying its major driver has been complicated by the complexity of the processes involved. Here, by taking a time-resolved transcriptomics-based approach, we assessed the engagement of 5 key cell types in the regenerative process. We compared the kinetics of transcriptional change taking place during regeneration in WT and CCR2KO mice and confirmed the disruption of normal FAP

Figure 5. FAP-derived VEGFA is critical after ischemic damage

(A–C) Representative images of vessels (CD31), adipocytes (perilipin), and collagen (collagen1) and necrosis (immunoglobulin G1 [IgG1]) in skeletal muscle collected from WT, $MP^{VEGFAKO}$, and $FAP^{VEGFAKO}$ mice 14 days after Fem Lig (scale bar of the large images, 250 μm; scale bar of the insets, 20–50 μm).

(D) H&E staining of skeletal muscles collected from WT, $MP^{VEGFAKO}$, and $FAP^{VEGFAKO}$ mice 14 days after Fem Lig (scale bar, 50 μm).

(E and F) Quantification of adipose tissue and extent of necrosis based on perilipin and IgG1 staining, respectively (n = 3–8, data represent the mean ± SEM, one-way ANOVA with multiple comparisons; $^{*}p < 0.05$, $^{**}p < 0.01$, $^{***}p < 0.001$).

(G) Quantification of muscle fiber cross-sectional area 14 days after Fem Lig (for skeletal muscle fiber, n = 3–4; data represent the mean ± SEM, one-way ANOVA, $^{*}p < 0.05$).

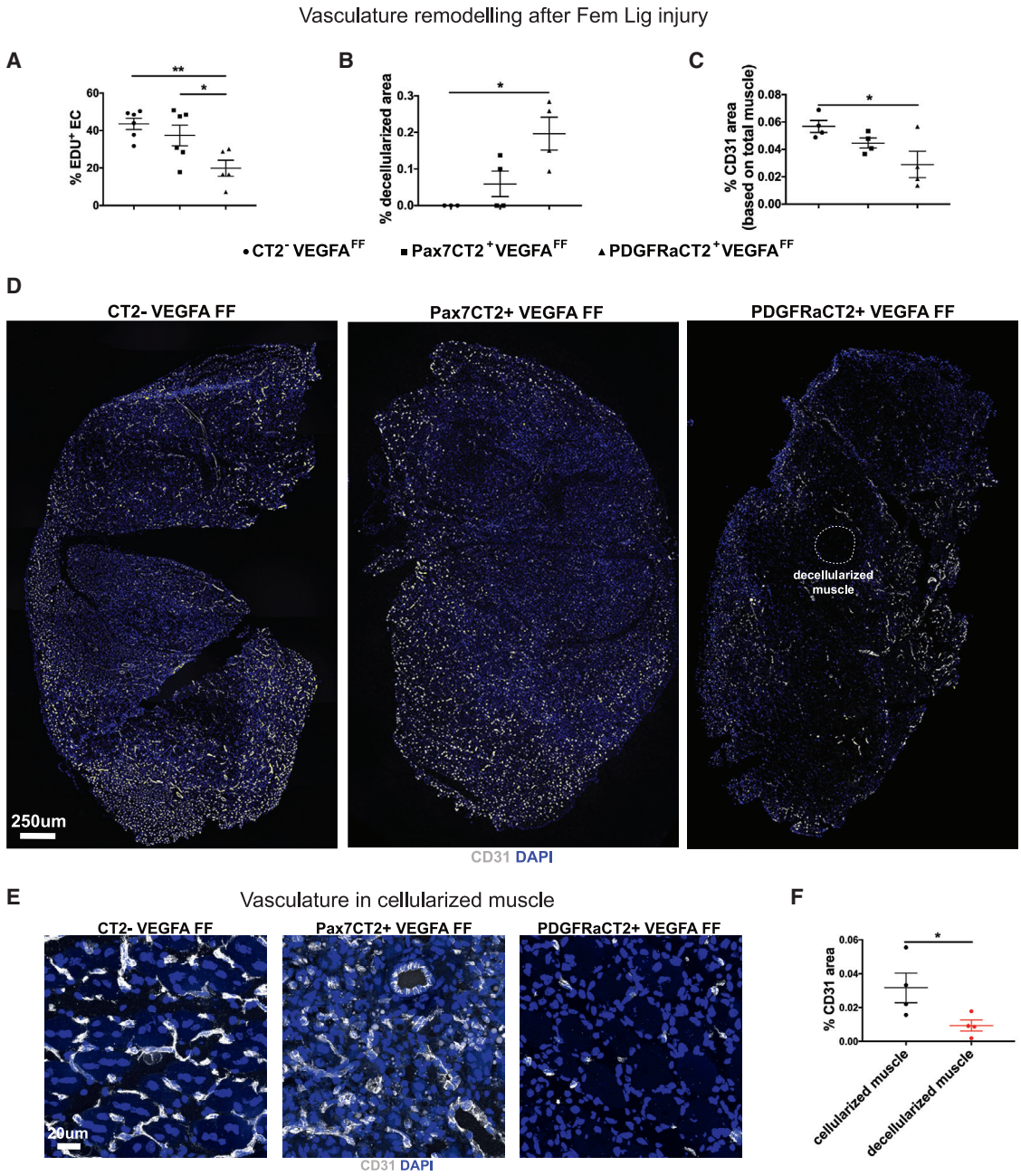

Figure 6. VEGFA depletion in FAPs, but not in MPs, affected vascular proliferation after ischemic damage

(A) EdU incorporation in ECs sorted from skeletal muscles of WT, $MP^{VEGFAKO}$, and $FAP^{VEGFAKO}$ mice 4 days after ischemic injury and 24 h after EdU treatment (n = 5–6, data represent the mean ± SEM, one-way ANOVA with multiple comparisons; *p < 0.05, **p < 0.01).

(B and C) Histological quantification of decellularized and vascularized areas in skeletal muscles collected from WT, $MP^{VEGFAKO}$, and $FAP^{VEGFAKO}$ mice 7 days after NTX (n = 4, data represent the mean ± SEM, one-way ANOVA with multiple comparisons, *p < 0.05).

(D and E) Representative images of skeletal muscles collected from WT, $MP^{VEGFAKO}$, and $FAP^{VEGFAKO}$ mice 7 days after ischemic injury (scale bar of the large images, 250 μm; scale bar of the insets, 20 μm).

(F) Histological quantification of vasculature in cellularized and decellularized areas in muscles collected from $FAP^{VEGFAKO}$ mice 7 days post damage (n = 4, data represent the mean ± SEM, Kruskal-Wallis test, *p < 0.05).

kinetics we reported previously. In addition, we found the lack of immune cell infiltration to have a drastic impact on ECs. A transcriptomics-based model of cellular interactions was built and not surprisingly pointed to VEGFA as a key determinant of endothelial activity. These predictions, that vessel remodeling was disrupted in CCR2KO animals and specifically that lack of VEGFA

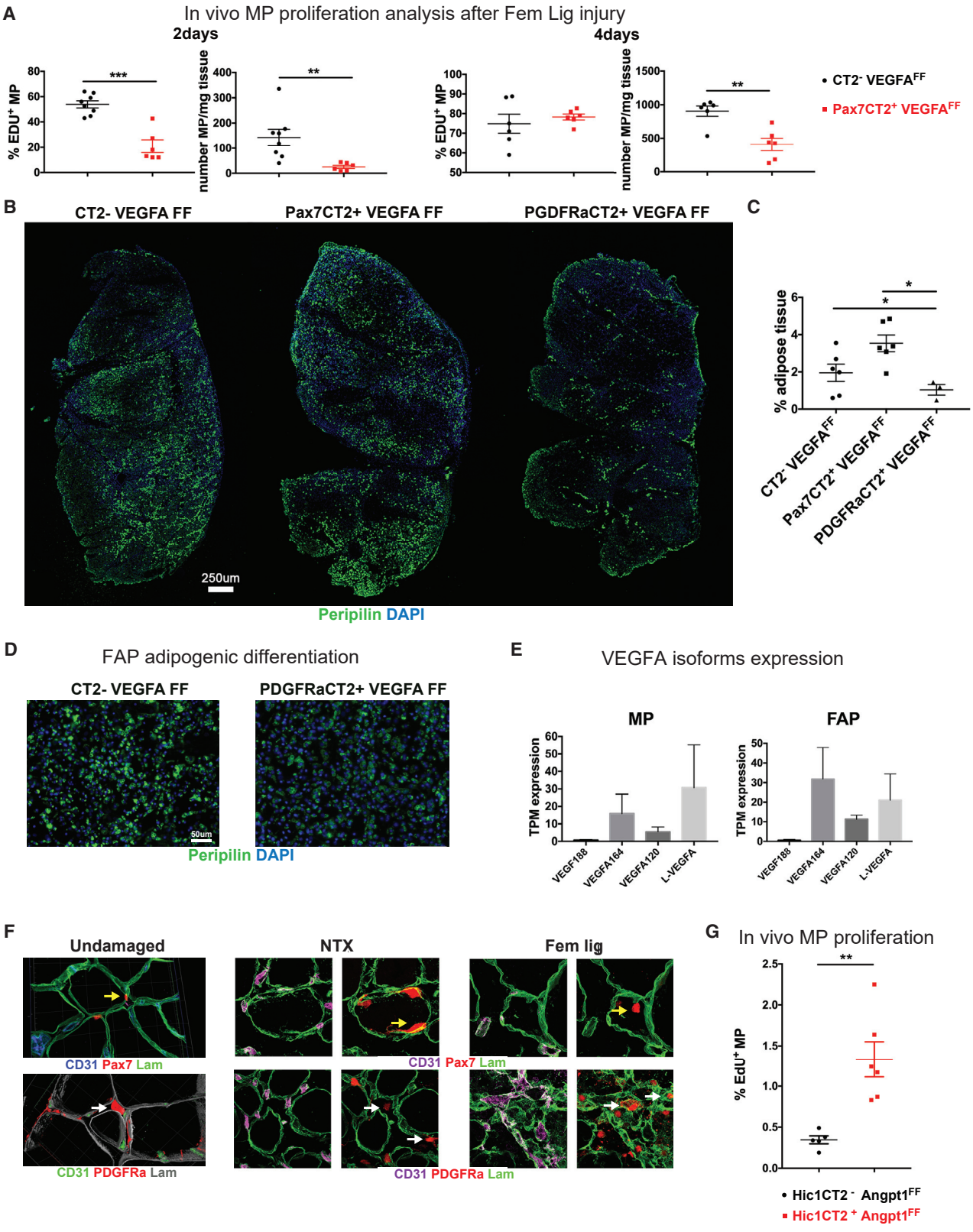

(legend on next page)

from ICs was a key determinant of this phenotype, were verified experimentally. Indeed, knocking out VEGFA from ICs was sufficient to lead to a phenotype vastly overlapping that of CCR2KO animals, including the muscle regeneration impairment but much reduced fibrosis/fat infiltration, which is likely due to a TNF-mediated direct effect on FAPs, as we reported previously.[18]

However, our interactome model also raised new questions by revealing that VEGFA was produced in comparable amounts by not just ICs, but also myogenic and stromal progenitors, all of which reside in close proximity to ECs. This promiscuity was not limited to VEGFA because more than three-quarters of all examined ligands had multiple cellular sources within regenerating muscle, displaying a level of redundancy in specific pathways across different cell types analogous to those described in other recent studies[1] and suggesting that this redundancy underlies a general strategy in biology. This prompted the question of whether the observed VEGFA expression pattern in muscle regeneration represents true redundancy, in which a given factor carries out the same functions independent of which cell produced it or, conversely, the cellular origin of a secreted molecule dictates its function in the context of the tissue. While the activity of redundant receptors can be validated bioinformatically,[35,44] such as in our analysis of VEGFR2 (*Kdr*) in ECs and MPs, understanding the functionality of a ligand produced by multiple sources cannot be investigated computationally. Thus, we generated additional mouse strains in which VEGFA was deleted specifically from MPs and FAPs, the two cell types beyond ICs that also produce it during regeneration.

Overall, our results show that VEGFA has multiple roles during muscle regeneration and that these functions are tightly linked with the cell type that produces it. The type of damage inflicted determines which of these functions, and therefore sources, are critical. In particular, VEGFA from FAPs is dispensable in non-ischemic damage models, such as myotoxin injury, but it is critical for the vascular remodeling that takes place after an ischemic event. Likely, the reason for this is that myotoxin injury induces a relatively mild angiogenic response compared with ischemic trauma.[45] Thus, VEGFA produced by ICs is sufficient to preserve the vasculature after NTX injection. However, in cases of severe ischemic damage, additional sources of VEGFA are required for a robust vascular response, and FAP-derived VEGFA becomes crucial.

Most importantly, our data indicate that the target of VEGFA signaling is specified by the cell type of origin. Thus, VEGFA from MPs acts in an autocrine fashion to support the early proliferation of these cells in ischemic and myotoxin damage models but is dispensable for vascular remodeling. We did not investigate the mechanism with which VEGFA affects myogenic stem cell activity early after damage, but its ability to modulate symmetric versus asymmetric divisions, as described by Chen et al.,[46] is likely to be involved. Surprisingly, despite the close proximity of myogenic and stromal cells *in situ* and the fact that they produce similar amounts of the protein, VEGFA from MPs cannot rescue the lack of VEGFA from FAPs and vice versa. Thus, signaling networks that appear to be shared across multiple cell types based on expression data are in reality compartmentalized in adult tissues, and the ability of one cell to signal to another cell is tightly controlled.

Hypothetically, this level of control could stem from the integration of antagonistic signaling pathways within the target cells, by which a given cell type may be unresponsive to a secreted factor even when the latter is present in the extracellular space and capable of engaging its receptors. However, we clearly show that MPs can respond to autocrine VEGFA, and a pro-angiogenic effect of MPs is readily observed when co-cultured with ECs.[47,48]

Alternatively, secreted factors could be prevented from reaching a specific target cell by anatomical barriers to its diffusion. Indeed, the importance of muscle architectural organization was elegantly demonstrated in the work by Webster et al.,[49] where intravital imaging was used to show that the myofiber's BM remains intact after the damaged fiber itself has been removed (ghost fibers) to guide *de novo* myogenesis. Activated MPs are in constant contact with the interior surface of these ghost fibers and are therefore essentially trapped in them. Our data suggest that such a barrier prevents MP-expressed VEGFA from reaching the endothelium, which is consistent with the notion that VEGFA can be locally constrained through anchoring to the ECM via its heparin binding domain.[50] Indeed, previous works have described how VEGFA isoforms capable of diffusing freely within their microenvironment induce vascular remodeling that is markedly different compared with VEGFA isoforms that remain anchored in the ECM.

In the past, exogenous delivery of VEGFA by adeno-associated viruses has shown an effect on muscle regeneration, but this system did not investigate the role of endogenous VEGFA and did not draw any conclusion about a potential autocrine role of VEGFA on MPs.[51,52]

Using an MP-specific *ad hoc* VEGFA depletion model, Verma et al.[2] described how VEGFA produced by MPs can interact with ECs, which, in turn, communicate via Notch signaling to regulate MP quiescence and vascular proximity. Although our data align regarding the importance of VEGFA signaling in regeneration and its critical effect on maintenance of proper MP activity and

Figure 7. Spatial compartmentalization of signaling imparts source-specific functions on secreted factors

(A) EdU incorporation in MPs sorted from skeletal muscles of WT, $MP^{VEGFAKO}$, and $FAP^{VEGFAKO}$ mice 2 and 4 days after ischemic and 24 h after EdU treatment (n = 6–8, data represent the mean ± SEM, unpaired t test or Mann-Whitney test; $^{**}p < 0.01$, $^{***}p < 0.001$).

(B and C) Histological staining of adipocytes (perilipin) and its quantification from skeletal muscles of WT, $MP^{VEGFAKO}$, and $FAP^{VEGFAKO}$ mice 5 days after ischemic injury (scale bar, 250 μm; n = 3–6, data represent the mean ± SEM, one-way ANOVA, $^{*}p < 0.05$).

(D) *In vitro* adipogenic differentiation of FAPs sorted from uninjured WT and $FAP^{VEGFAKO}$ mice; adipogenesis was identified with perilipin staining (scale bar, 50 μm).

(E) Expression of VEGFA isoforms by MPs and FAPs purified from undamaged WT skeletal muscles.

(F) Histological staining of laminin (Lam), vessels (CD31), FAPs (PDGFRa), and MPs (Pax7) in uninjured and myotoxin- and ischemia-damaged WT skeletal muscles.

(G) EdU incorporation in MPs purified from skeletal muscles of WT ($Hic1CT2^{-}Angpt1^{FF}$) and Angpt1 KO ($Hic1CT2^{+}Angpt1^{FF}$) animals 3 weeks after Angpt1 depletion.

numbers, our conclusions regarding the signaling networks through which it acts differ. Indeed, while Verma et al.[2] describe FAPs to be an equally viable source of VEGFA compared with MPs, in their experiments, like in our hands, FAP-derived VEGFA fails to rescue the phenotype observed in MP-derived VEGFA depletion, reinforcing our confidence in the critical role of signal compartmentalization in this system.

Although current bioinformatics approaches provide outstanding tools to predict Lig-Rec pairing, our work clearly shows that not all signaling interactions can be predicted based on expression data alone because additional factors should be kept in mind when modeling muscle regeneration. Here, we describe how the presence of structural barriers and the type/severity of damage are important elements. We propose that the interposition of stable, matrix-rich structures like the BM can limit the diffusion of signaling molecules, thus assigning distinct roles to cell subsets secreting the same ligand. In addition, the type of injury can also modify such structural barriers, thus shaping cell signaling. First, the damage itself can have a direct impact on re-organization of the BM, as observed in our systems, where ECs and FAPs are separated by the BM after toxic injury, but they are completely embedded in the same BM layer after ischemic damage. Second, the cellular target of the injury also dictates its consequences. In direct myotoxic damage (NTX), which affects only muscle fibers, circulating ICs are recruited to the tissue through unperturbed blood vessels, where they provide cytokines to regulate vascular remodeling and controlling FAP activation.[53] In contrast, in an ischemic injury, ICs infiltration might be reduced because of vessel impairment.[54] The different IC recruitment itself could cause a lack of factors that lead to compensating signaling mechanisms. In our system, after NTX injury, VEGFA is provided by ICs to promote vascular remodeling, whereas FAP-derived VEGFA is dispensable. The situation is completely different after Fem Lig damage, where damage to blood vessels is more extensive, and VEGFA by FAPs becomes pivotal for muscle repair, probably because of an increased requirement for this factor.

Inclusion of these parameters, and surely others yet to be defined, will be required to more faithfully represent and predict the behavior of complex cellular systems in the future. Computational modeling is now part of many attempts to faithfully describe biological systems. However, it invariably considers biological networks in a homogeneous spatial environment. Incorporating structural features into these mathematical models is a new area of research.[55] This could be integrated with innovative multiplex imaging able to simultaneously profile the spatial distribution of cell surface, intracellular, and ECM proteins.[41]

Finally, it is interesting to speculate that the compartmentalization of signaling described here is one of the factors that allows the same pathways to be re-utilized in multiple distinct biological processes.

Limitations of the study

In our analysis of RNA-seq, time point tests were unbalanced between conditions; i.e., WT and CCR2KO systems. This could lead to misleading clustering assignments. Therefore, our hypothesis and conclusions were drawn by inspecting all time points tested during the entire regeneration process.

In the current study, we also did not include factors expressed by myofibers (e.g., VEGFA). However, when this factor was specifically deleted in adult myofibers, the only reported effect was mainly on the myofiber's ability to respond to exercise. No change in vascular density was seen, supporting our hypothesis that, in adult tissue, VEGF cannot act outside of the BM.[29]

Another limitation of our work could be the lack of detection of secreted VEGFA localized within the tissue to verify that its distribution is different across the various VEGFA KO animals. Highly sensitive methods to detect secreted factors in tissue sections as well as new technologies (for example, CODEX imaging) were unsuccessful. Generation of *ad hoc* transgenic mice might be the only way to allow VEGFA detection *in vivo*.

STAR★METHODS

Detailed methods are provided in the online version of this paper and include the following:

- KEY RESOURCES TABLE
- RESOURCE AVAILABILITY
  - Lead contact
  - Materials availability
  - Data and code availability
- EXPERIMENTAL MODEL AND SUBJECT DETAILS
  - *In vivo* mouse models
  - Myogenic progenitors primary culture
  - Fibro/adipogenic progenitors primary culture
- METHOD DETAILS
  - Skeletal muscle injury models
  - Tissue digestion and cell purification after notexin damage
  - RNA extractions from sorted cell populations
  - Perfusion and tissue collection
  - Immunofluorescent staining on frozen sections
  - Cytospinned cells and staining
  - Myogenic cell immunofluorescence and TUNEL staining on frozen sections
  - H&E staining
  - Image acquisition
  - Histological quantification
  - Multiplexed immunofluorescence co-detection (CODEX)
  - Perilipin staining
  - VEGFA ELISA experiment
  - Fluorescent activated cell sorting (FACS) analysis
  - RNASeq bioinformatics analyses
  - Differential expression analysis
- QUANTIFICATION AND STATISTICAL ANALYSIS

SUPPLEMENTAL INFORMATION

Supplemental information can be found online at https://doi.org/10.1016/j.celrep.2023.112051.

ACKNOWLEDGMENTS

This work was supported by CIHR grant FDN-159908 (to F.M.V.R.) and CIHR grant 472535 (to M.T.). We thank the BRC-seq, UBC FACS, AbLab, BRC

genotyping and transgenic units, David Guo, and Lucas Rempel for technical assistance as well as Simone Morandi for the graphical abstract.

AUTHOR CONTRIBUTIONS

All authors were responsible for performing experiments and analyses. E.G., P.M., N.D., M.T., and F.M.V.R. were involved in experimental design, data interpretation, and preparation of the manuscript. E.G., P.M., N.D., M.T., M.S.H., C.E., and F.M.V.R. were involved in editing the manuscript.

DECLARATION OF INTERESTS

The authors declare no competing interests.

Received: October 4, 2020
Revised: September 8, 2022
Accepted: January 16, 2023
Published: January 31, 2023

REFERENCES

1. Rezza, A., Wang, Z., Sennett, R., Qiao, W., Wang, D., Heitman, N., Mok, K.W., Clavel, C., Yi, R., Zandstra, P., et al. (2016). Signaling networks among stem cell precursors, transit-amplifying progenitors, and their niche in developing hair follicles. Cell Rep. *14*, 3001–3018.
2. Verma, M., Asakura, Y., Murakonda, B.S.R., Pengo, T., Latroche, C., Chazaud, B., McLoon, L.K., and Asakura, A. (2018). Muscle satellite cell cross-talk with a vascular niche maintains quiescence via VEGF and Notch signaling. Cell Stem Cell *23*, 530–543.e9.
3. Zhou, J.X., Taramelli, R., Pedrini, E., Knijnenburg, T., and Huang, S. (2017). Extracting intercellular signaling network of cancer tissues using ligand-receptor expression patterns from whole-tumor and single-cell transcriptomes. Sci. Rep. *7*, 8815.
4. Kumar, M.P., Du, J., Lagoudas, G., Jiao, Y., Sawyer, A., Drummond, D.C., Lauffenburger, D.A., and Raue, A. (2018). Analysis of single-cell RNA-seq identifies cell-cell communication associated with tumor characteristics. Cell Rep. *25*, 1458–1468.e4.
5. Efremova, M., Vento-Tormo, M., Teichmann, S.A., and Vento-Tormo, R. (2020). CellPhoneDB: inferring cell–cell communication from combined expression of multi-subunit ligand–receptor complexes. Nat. Protoc. *15*, 1484–1506. https://doi.org/10.1038/s41596-020-0292-x.
6. Choi, H., Sheng, J., Gao, D., Li, F., Durrans, A., Ryu, S., Lee, S.B., Narula, N., Rafii, S., Elemento, O., et al. (2015). Transcriptome analysis of individual stromal cell populations identifies stroma-tumor crosstalk in mouse lung cancer model. Cell Rep. *10*, 1187–1201.
7. Mukund, K., and Subramaniam, S. (2020). Skeletal muscle: a review of molecular structure and function, in health and disease health and disease models of systems properties and processes > cellular models. WIREs Mechanisms. of. Disease. *12*.
8. Babbs, A., Chatzopoulou, M., Edwards, B., Squire, S.E., Wilkinson, I.V.L., Wynne, G.M., Russell, A.J., and Davies, K.E. (2020). From diagnosis to therapy in Duchenne muscular dystrophy. Biochem. Soc. Trans. *48*, 813–821.
9. Carosio, S., Berardinelli, M.G., Aucello, M., and Musarò, A. (2011). Impact of ageing on muscle cell regeneration. Ageing Res. Rev. *10*, 35–42.
10. Arnold, L., Henry, A., Poron, F., Baba-Amer, Y., van Rooijen, N., Plonquet, A., Gherardi, R.K., and Chazaud, B. (2007). Inflammatory monocytes recruited after skeletal muscle injury switch into antiinflammatory macrophages to support myogenesis. J. Exp. Med. *204*, 1057–1069.
11. Christov, C., Chrétien, F., Abou-Khalil, R., Bassez, G., Vallet, G., Authier, F.J., Bassaglia, Y., Shinin, V., Tajbakhsh, S., Chazaud, B., and Gherardi, R.K. (2007). Muscle satellite cells and endothelial cells: close neighbors and privileged partners. Mol. Biol. Cell *18*, 1397–1409.
12. Dammone, G., Karaz, S., Lukjanenko, L., Winkler, C., Sizzano, F., Jacot, G., Migliavacca, E., Palini, A., Desvergne, B., Gilardi, F., and Feige, J.N. (2018). PPARγ controls ectopic adipogenesis and cross-talks with myogenesis during skeletal muscle regeneration. Int. J. Mol. Sci. *19*, 2044. https://doi.org/10.3390/ijms19072044.
13. Fiore, D., Judson, R.N., Low, M., Lee, S., Zhang, E., Hopkins, C., Xu, P., Lenzi, A., Rossi, F.M.V., and Lemos, D.R. (2016). Pharmacological blockage of fibro/adipogenic progenitor expansion and suppression of regenerative fibrogenesis is associated with impaired skeletal muscle regeneration. Stem Cell Res. *17*, 161–169.
14. Theret, M., Gsaier, L., Schaffer, B., Juban, G., Ben Larbi, S., Weiss-Gayet, M., Bultot, L., Collodet, C., Foretz, M., Desplanches, D., et al. (2017). AMPKα1-LDH pathway regulates muscle stem cell self-renewal by controlling metabolic homeostasis. EMBO J. *36*, 1946–1962.
15. Joe, A.W.B., Yi, L., Natarajan, A., Le Grand, F., So, L., Wang, J., Rudnicki, M.A., and Rossi, F.M.V. (2010). Muscle injury activates resident fibro/adipogenic progenitors that facilitate myogenesis. Nat. Cell Biol. *12*, 153–163.
16. Kostallari, E., Baba-Amer, Y., Alonso-Martin, S., Ngoh, P., Relaix, F., Lafuste, P., and Gherardi, R.K. (2015). Pericytes in the myovascular niche promote post-natal myofiber growth and satellite cell quiescence. Development *142*, 1242–1253.
17. Latroche, C., Weiss-Gayet, M., Muller, L., Gitiaux, C., Leblanc, P., Liot, S., Ben-Larbi, S., Abou-Khalil, R., Verger, N., Bardot, P., et al. (2017). Coupling between myogenesis and angiogenesis during skeletal muscle regeneration is stimulated by restorative macrophages. Stem Cell Rep. *9*, 2018–2033.
18. Lemos, D.R., Babaeijandaghi, F., Low, M., Chang, C.K., Lee, S.T., Fiore, D., Zhang, R.H., Natarajan, A., Nedospasov, S.A., and Rossi, F.M.V. (2015). Nilotinib reduces muscle fibrosis in chronic muscle injury by promoting TNF-mediated apoptosis of fibro/adipogenic progenitors. Nat. Med. *21*, 786–794.
19. Mojumdar, K., Liang, F., Giordano, C., Lemaire, C., Danialou, G., Okazaki, T., Bourdon, J., Rafei, M., Galipeau, J., Divangahi, M., and Petrof, B.J. (2014). Inflammatory monocytes promote progression of Duchenne muscular dystrophy and can be therapeutically targeted via CCR 2. EMBO Mol. Med. *6*, 1476–1492.
20. Ochoa, O., Sun, D., Reyes-Reyna, S.M., Waite, L.L., Michalek, J.E., McManus, L.M., and Shireman, P.K. (2007). Delayed angiogenesis and VEGF production in CCR2-/- mice during impaired skeletal muscle regeneration. Am. J. Physiol. Regul. Integr. Comp. Physiol. *293*, R651–R661.
21. Saclier, M., Yacoub-Youssef, H., Mackey, A.L., Arnold, L., Ardjoune, H., Magnan, M., Sailhan, F., Chelly, J., Pavlath, G.K., Mounier, R., et al. (2013). Differentially activated macrophages orchestrate myogenic precursor cell fate during human skeletal muscle regeneration. Stem Cell. *31*, 384–396.
22. Uezumi, A., Fukada, S.I., Yamamoto, N., Takeda, S., and Tsuchida, K. (2010). Mesenchymal progenitors distinct from satellite cells contribute to ectopic fat cell formation in skeletal muscle. Nat. Cell Biol. *12*, 143–152.
23. Villalta, S.A., Rosenthal, W., Martinez, L., Kaur, A., Sparwasser, T., Tidball, J.G., Margeta, M., Spencer, M.J., and Bluestone, J.A. (2014). Regulatory T cells suppress muscle inflammation and injury in muscular dystrophy. Sci. Transl. Med. *6*, 258ra142.
24. Willenborg, S., Lucas, T., van Loo, G., Knipper, J.A., Krieg, T., Haase, I., Brachvogel, B., Hammerschmidt, M., Nagy, A., Ferrara, N., et al. (2012). CCR2 recruits an inflammatory macrophage subpopulation critical for angiogenesis in tissue repair. Blood *120*, 613–625.
25. Wosczyna, M.N., Konishi, C.T., Perez Carbajal, E.E., Wang, T.T., Walsh, R.A., Gan, Q., Wagner, M.W., and Rando, T.A. (2019). Mesenchymal stromal cells are required for regeneration and homeostatic maintenance of skeletal muscle. Cell Rep. *27*, 2029–2035.e5.
26. Zhang, J., Muri, J., Fitzgerald, G., Gorski, T., Gianni-Barrera, R., Masschelein, E., D'Hulst, G., Gilardoni, P., Turiel, G., Fan, Z., et al. (2020). Endothelial lactate controls muscle regeneration from ischemia by inducing M2-like macrophage polarization. Cell Metab. *31*, 1136–1153.e7.

27. Sobral-Reyes, M.F., and Lemos, D.R. (2020). Recapitulating human tissue damage, repair and fibrosis with hPSC-derived organoids: concise review. Stem Cells *38*, 318–329.

28. Scott, R.W., Arostegui, M., Schweitzer, R., Rossi, F.M.V., and Underhill, T.M. (2019). Hic1 defines quiescent mesenchymal progenitor subpopulations with distinct functions and fates in skeletal muscle regeneration. Cell Stem Cell *25*, 797–813.e9.

29. Knapp, A.E., Goldberg, D., Delavar, H., Trisko, B.M., Tang, K., Hogan, M.C., Wagner, P.D., and Breen, E.C. (2016). Skeletal myofiber VEGF regulates contraction-induced perfusion and exercise capacity but not muscle capillarity in adult mice. Am. J. Physiol. Regul. Integr. Comp. Physiol. *311*, R192–R199.

30. Huey, K.A., Smith, S.A., Sulaeman, A., and Breen, E.C. (2016). Skeletal myofiber VEGF is necessary for myogenic and contractile adaptations to functional overload of the plantaris in adult mice. J. Appl. Physiol. *120*, 188–195.

31. Lu, C.Y., Santosa, K.B., Jablonka-Shariff, A., Vannucci, B., Fuchs, A., Turnbull, I., Pan, D., Wood, M.D., and Snyder-Warwick, A.K. (2020). Macrophage-derived vascular endothelial growth factor-A is integral to neuromuscular junction reinnervation after nerve injury. J. Neurosci. *40*, 9602–9616.

32. De Micheli, A.J., Laurilliard, E.J., Heinke, C.L., Ravichandran, H., Fraczek, P., Soueid-Baumgarten, S., De Vlaminck, I., Elemento, O., and Cosgrove, B.D. (2020). Single-cell analysis of the muscle stem cell hierarchy identifies heterotypic communication signals involved in skeletal muscle regeneration. Cell Rep. *30*, 3583–3595.e5.

33. Dmitrijeva, M., Ossowski, S., Serrano, L., and Schaefer, M.H. (2018). Tissue-specific DNA methylation loss during ageing and carcinogenesis is linked to chromosome structure, replication timing and cell division rates. Nucleic Acids Res. *46*, 7022–7039.

34. Verma, M., Asakura, Y., Wang, X., Zhou, K., Ünverdi, M., Kann, A.P., Krauss, R.S., and Asakura, A. (2021). Endothelial cell signature in muscle stem cells validated by VEGFA-FLT1-AKT1 axis promoting survival of muscle stem cell. Preprint at bioRxiv. https://doi.org/10.1101/2021.08.28.458037.

35. Martini, P., Sales, G., Calura, E., Cagnin, S., Chiogna, M., and Romualdi, C. (2014). TimeClip: pathway analysis for time course data without replicates. BMC Bioinformatics *15*, S3.

36. Santini, M.P., Malide, D., Hoffman, G., Pandey, G., D'Escamard, V., Nomura-Kitabayashi, A., Rovira, I., Kataoka, H., Ochando, J., Harvey, R.P., et al. (2020). Tissue-resident PDGFRα + progenitor cells contribute to fibrosis versus healing in a context- and spatiotemporally dependent manner. Cell Rep. *30*, 555–570.e7.

37. Almuraikhy, S., Kafienah, W., Bashah, M., Diboun, I., Jaganjac, M., Al-Khelaifi, F., Abdesselem, H., Mazloum, N.A., Alsayrafi, M., Mohamed-Ali, V., and Elrayess, M.A. (2016). Interleukin-6 induces impairment in human subcutaneous adipogenesis in obesity-associated insulin resistance. Diabetologia *59*, 2406–2416.

38. Moratal, C., Raffort, J., Arrighi, N., Rekima, S., Schaub, S., Dechesne, C.A., Chinetti, G., and Dani, C. (2018). IL-1β- and IL-4-polarized macrophages have opposite effects on adipogenesis of intramuscular fibro-adipogenic progenitors in humans. Sci. Rep. *8*, 17005.

39. Serrano, A.L., Baeza-Raja, B., Perdiguero, E., Jardí, M., and Muñoz-Cánoves, P. (2008). Interleukin-6 is an essential regulator of satellite cell-mediated skeletal muscle hypertrophy. Cell Metab. *7*, 33–44.

40. Tee, M.K., and Jaffe, R.B. (2001). A precursor form of vascular endothelial growth factor arises by initiation from an upstream in-frame CUG codon. Biochem. J. *359*, 219–226.

41. Wang, Y.X., Holbrook, C.A., Hamilton, J.N., Garoussian, J., Afshar, M., Su, S., Schürch, C.M., Lee, M.Y., Goltsev, Y., Kundaje, A., Nolan, G.P., and Blau, H.M. (2022). A single cell spatial temporal atlas of skeletal muscle reveals cellular neighborhoods that orchestrate regeneration and become disrupted in aging. Preprint at bioRxiv. https://doi.org/10.1101/2022.06.10.494732.

42. Abou-Khalil, R., Le Grand, F., Pallafacchina, G., Valable, S., Authier, F.J., Rudnicki, M.A., Gherardi, R.K., Germain, S., Chretien, F., Sotiropoulos, A., et al. (2009). Autocrine and paracrine Angiopoietin 1/Tie-2 signaling promotes muscle satellite cell self-renewal. Cell Stem Cell *5*, 298–309.

43. Groppa, E., Brkic, S., Bovo, E., Reginato, S., Sacchi, V., Maggio, N.D., Muraro, M.G., Calabrese, D., Heberer, M., Gianni-Barrera, R., and Banfi, A. (2015). VEGF dose regulates vascular stabilization through Semaphorin3A and the Neuropilin-1 + monocyte/TGF-b1 paracrine axis. https://doi.org/10.15252/emmm.201405003.

44. Alvarez, M.J., Shen, Y., Giorgi, F.M., Lachmann, A., Ding, B.B., Ye, B.H., and Califano, A. (2016). Functional characterization of somatic mutations in cancer using network-based inference of protein activity. Nat. Genet. *48*, 838–847.

45. Plant, D.R., Colarossi, F.E., and Lynch, G.S. (2006). Notexin causes greater myotoxic damage and slower functional repair in mouse skeletal muscles than bupivacaine. Muscle Nerve *34*, 577–585.

46. Chen, W., Wang, Y.X., Ritso, M., Perkins, T.J., and Rudnicki, M.A. (2022). KDR signaling in muscle stem cells promotes asymmetric division and progenitor generation for efficient regeneration. Preprint at bioRxiv. https://doi.org/10.1101/2022.06.27.497734.

47. Rhoads, R.P., Flann, K.L., Cardinal, T.R., Rathbone, C.R., Liu, X., and Allen, R.E. (2013). Satellite cells isolated from aged or dystrophic muscle exhibit a reduced capacity to promote angiogenesis in vitro. Biochem. Biophys. Res. Commun. *440*, 399–404.

48. Mettouchi, A. (2012). Cell Adhesion & Migration the role of extracellular matrix in vascular branching morphogenesis the role of extracellular matrix in vascular branching morphogenesis. https://doi.org/10.4161/cam.22862.

49. Webster, M.T., Manor, U., Lippincott-Schwartz, J., and Fan, C.M. (2016). Intravital imaging reveals ghost fibers as architectural units guiding myogenic progenitors during regeneration. Cell Stem Cell *18*, 243–252.

50. Ruhrberg, C., Gerhardt, H., Golding, M., Watson, R., Ioannidou, S., Fujisawa, H., Betsholtz, C., and Shima, D.T. (2002). Spatially restricted patterning cues provided by heparin-binding VEGF-A control blood vessel branching morphogenesis. Genes Dev. *16*, 2684–2698.

51. Arsic, N., Zacchigna, S., Zentilin, L., Ramirez-Correa, G., Pattarini, L., Salvi, A., Sinagra, G., and Giacca, M. (2004). Vascular endothelial growth factor stimulates skeletal muscle regeneration in vivo. Mol. Ther. *10*, 844–854.

52. Messina, S., Mazzeo, A., Bitto, A., Aguennouz, M., Migliorato, A., De Pasquale, M.G., Minutoli, L., Altavilla, D., Zentilin, L., Giacca, M., et al. (2007). VEGF overexpression via adeno-associated virus gene transfer promotes skeletal muscle regeneration and enhances muscle function in mdx mice. FASEB J. *21*, 3737–3746.

53. Theret, M., Saclier, M., Messina, G., and Rossi, F.M.V. (2022). Macrophages in skeletal muscle dystrophies, an entangled partner. J. Neuromuscul. Dis. *9*, 1–23.

54. Germani, A., Di Carlo, A., Mangoni, A., Straino, S., Giacinti, C., Turrini, P., Biglioli, P., and Capogrossi, M.C. (2003). Vascular endothelial growth factor modulates skeletal myoblast function. Am. J. Pathol. *163*, 1417–1428.

55. Getz, M.C., Nirody, J.A., and Rangamani, P. (2018). Stability analysis in spatial modeling of cell signaling. WIREs Mechanisms. of. Disease. *10*, e1395.

56. Padgett, M.E., McCord, T.J., McClung, J.M., and Kontos, C.D. (2016). Methods for acute and subacute murine hindlimb ischemia. J. Vis. Exp. *2016*, e54166.

57. Palla, A.R., Ravichandran, M., Wang, Y.X., Alexandrova, L., Yang, A.V., Kraft, P., Holbrook, C.A., Schürch, C.M., Ho, A.T.V., and Blau, H.M. (2021). Inhibition of prostaglandin-degrading enzyme 15-PGDH rejuvenates aged muscle mass and strength. Science *371*, eabc8059.

58. Risso, D., Ngai, J., Speed, T.P., and Dudoit, S. (2014). Normalization of RNA-seq data using factor analysis of control genes or samples. Nat. Biotechnol. *32*, 896–902.

59. Charrad, M., Ghazzali, N., Boiteau, V., and Niknafs, A. (2014). Nbclust: an R package for determining the relevant number of clusters in a data set. J. Stat. Softw. *61*, 1–36.

60. Brock, G., Pihur, V., Datta, S., and Datta, S. (2008). clValid: an R package for cluster validation. J. Stat. Softw. *25*, 1–22.

61. Robinson, M.D., Mccarthy, D.J., and Smyth, G.K. (2010). edgeR: a Bioconductor package for differential expression analysis of digital gene expression data. Bioinformatics *26*, 139–140.

62. Müssel, C., Hopfensitz, M., and Kestler, H.A. (2010). BoolNet-an R package for generation, reconstruction and analysis of Boolean networks. Bioinformatics *26*, 1378–1380.

63. Yu, G., Wang, L.G., Han, Y., and He, Q.Y. (2012). ClusterProfiler: an R package for comparing biological themes among gene clusters. OMICS *16*, 284–287.

64. Sales, G., Calura, E., and Romualdi, C. (2019). Meta Graphite-a new layer of pathway annotation to get metabolite networks. Bioinformatics *35*, 1258–1260.

65. Yang, Z., Wong, A., Kuh, D., Paul, D.S., Rakyan, V.K., Leslie, R.D., Zheng, S.C., Widschwendter, M., Beck, S., and Teschendorff, A.E. (2016). Correlation of an epigenetic mitotic clock with cancer risk. Genome Biol. *17*, 205.

STAR★METHODS

KEY RESOURCES TABLE

REAGENT or RESOURCE	SOURCE	IDENTIFIER
Antibodies		
FITC anti-CD45	AbLab	Clone I3/2
APC anti-CD45	AbLab	Clone I3/2
FITC anti-CD31	eBioscience	Clone 390
APC anti-CD31	eBioscience	Clone 390
PECy7 anti-Sca1	eBioscience	Clone D7
biotinylated anti-VCAM	AbLab	Clone 429 MVCAM.A
streptavidin-PE	Caltag Laboratories	Cat #SA1004-4
APC anti-α7integrin	AbLab	Clone R2F2
rabbit anti-laminin	Abcam	Cat #15575
Myogenin	AbLab	Clone F5D
Desmin	Abcam	Cat #ab6322
mouse anti-collagen	Abcam	Cat #ab90395
rat anti-CD31	Biolegend	Clone 390
goat anti-CD31	R&D	Cat #AF3628
rabbit anti-perilipin	Abcam	Cat #ab3526
rabbit anti-MyoD	Abcam	Cat #ab133627
mouse anti-Pax7	AbLab	Clone 1/10
rabbit anti-VEGFA	Abcam	Cat #ab52917
donkey anti-rabbit 488	Invitrogen	Cat #A21206
donkey anti-goat 488	Invitrogen	Cat #A11055
donkey anti-rabbit 647	Invitrogen	Cat #A31573
donkey anti-goat 647	Life Technologies	Cat #A21447
goat anti-rabbit 488	Life Technologies	Cat #A11034
goat anti-rat 488	Invitrogen	Cat #A11006
goat anti-rabbit 647	Invitrogen	Cat #A21245
donkey anti-mouse IgG1	Life Technologies	Cat #1305303
goat anti-mouse IgG1 Alexa 488	Thermo Fisher	Cat #A21121
Chemicals, peptides, and recombinant proteins		
Hoechst 33342	Sigma Aldrich	Cat #B2261
RNAzol	Sigma Aldrich	Cat #R4533
Dextran-Texas Red	Invitrogen	Cat #D1864
Lectin-fluorescein isothiocyanate	Sigma Aldrich	Cat #L0401
Sodium Borohydride	Sigma Aldrich	Cat #213462
Critical commercial assays		
Ethidium Bromide kit	Thermo Fisher	Cat #C10337
VEGFA ELISA kit	R&D systems	Cat #MMV00
TUNEL staining kit	ABP Biosciences	Cat #A052
Deposited data		
RNASeq data	This paper	GEO: GSE210748
Experimental models: Organisms/strains		
B6.Cg-Pax7$^{tm1(cre/ERT2)Gaka}$/J	The Jackson Laboratory	stock number 017763
Pdgfra^{CreERT2}	Gift from Dr. Brigid Hogan	
Tg(VAV1-cre)1Graf	The Jackson Laboratory	stock number 127936

(*Continued on next page*)

Continued		
REAGENT or RESOURCE	SOURCE	IDENTIFIER
B6.Cg-Gt(ROSA) 26Sor$^{tm14(CAG-tdTomato)Hze}$/J	The Jackson Laboratory	stock number 007914
VEGFa^{tm2Gne}	Gift from Dr. Richard Lang	
B6.129S4-Pdgfra$^{tm11(EGFP)Sor}$/J	The Jackson Laboratory	stock number 007669
Tg(Cspg4-DsRed.T1)1Akik/J	The Jackson Laboratory	stock number 008241
B6.129s4-ccr2^{TM1Ifc}/J	The Jackson Laboratory	stock number 004999
Other		
Original codes	This paper	https://doi.org/10.5281/zenodo.7501769

RESOURCE AVAILABILITY

Lead contact

Further information and requests for resources and reagents should be directed to and will be fulfilled by Dr. Elena Groppa (elena.groppa@hotmail.it) and Dr. Fabio Rossi (fabio@brc.ubc.ca).

Materials availability

This study did not generate new unique reagents.

Data and code availability

- RNASeq data have been deposited at GEO and are publicly available. Accession number is listed in the key resources table. Microscopy data reported in this paper will be shared by the lead contact upon request.
- All original code used has been deposited at Zenodo and is publicly available. Accession number is listed in the key resources table.
- Any additional information required to reanalyze the data reported in this paper is available from the lead contact upon request.

EXPERIMENTAL MODEL AND SUBJECT DETAILS

In vivo mouse models

Either B6.Cg-Pax7$^{tm1(cre/ERT2)Gaka}$/J (Jax stock number 017763) or Pdgfra^{CreERT2}mice (kind gift from Dr. Brigid Hogan) or Tg(VAV1-cre)1Graf (Jax stock number 127936) were crossed with B6.Cg-Gt(ROSA)26Sor$^{tm14(CAG-tdTomato)Hze}$/J (Jax stock number 007914) and VEGFa^{tm2Gne} (kindly provided by Dr. Richard Lang from Cincinnati Children's Hospital) to generate Pax7 CT2 or Pdgfra CT2 VEGFa$^{flox/flox}$ tdTomato mice. We used other mouse models like B6.129S4-Pdgfra$^{tm11(EGFP)Sor}$/J (Jax stock number 007669; here in referred to as Pdgfra eGFP) and Tg(Cspg4-DsRed.T1)1Akik/J (Jax stock number 008241; herein referred to as NG2 dsRed), which were maintained either in a wild type B6 background (PDGFRa EGFP WT and NG2 dsRed WT) or bred with B6.129s4-ccr2^{TM1Ifc}/J (CCR2KO): (Jax stock number 004999; herein referred to as CCR2KO) to generate PDGFRa EGFP CCR2KO. Mice were housed, in a pathogen free facility, under standard conditions (12 h light/dark cycle). All experiments conducted in accordance to ethical treatment standards of the Animal Care Committee at the University of British Columbia. Allelic recombination was induced by daily injections of 0.1 mg/g tamoxifen (TAM) in 100 μL of corn oil for 5 consecutive days, administered intraperitoneally to 8 weeks old animals. To control TAM toxicity, all mice including controls were subjected to experimental procedures 2 weeks after TAM to allow a washout period. Male and female mice were equally mixed in our experiments.

Myogenic progenitors primary culture

Myogenic progenitors (MPs) were extracted as described in the Method details session and sorted as CD45-/CD31-/Sca1-/a7integrin+/VCAM+. MP were purified from male and female mice equally mixed in our experiments.

Clonal assay and Myogenic differentiation were assessed as previously described.[14]

Cells were then cultured on a Matrigel®-coated (1:10, Corning #354234) 48 well-plate in proliferative media (Dulbecco's modified eagle medium (DMEM/F12; Thermo Fisher), 20% fetal bovine serum (FBS), 0.75 μg/mL bFGF (PeproTech), 1% Penicillin/Streptomycin (Thermo Fisher).

For clonal growth assay, sorted MPs were seeded at 50 cells per well in the proliferative media on a Matrigel®-coated 48 well plate and the number of clones and number of cells per each clone were quantified from 3 to 6 days after sort.

For differentiation assay, MPs were seeded at 3000 cells/cm^2 for expansion for 5–7 days in proliferation media on Matrigel-Coated plates. After a passage, cells were seeded at 30,000 cells/cm^2 in proliferative media for 6 h and then switched to a differentiation

media (DMEM/F12, 2% Horse Serum (Sigma Aldrich), 1% Penicillin/Streptomycin). The levels differentiation and fusions were assessed after 3 days. Cells were fixated in 4% paraformaldehyde (PFA) for 7 min, then incubated with blocking buffer (1X PBS, 3% Goat serum, 0.3% Triton X-100) for 1 h before being incubated overnight at 4°C with Myogenin (AbLab, clone F5D) and Desmin (Abcam #ab6322) antibodies. Then, cells were washed in phosphate buffered saline (PBS), incubated with secondaries antibodies (Invitrogen) and counterstained with 600nM DAPI for 5 min. The number of positive cells for Myogenin and number of nuclei per myotubes were then quantified.

Fibro/adipogenic progenitors primary culture

For *in vitro* differentiation studies, skeletal muscle from WT and $FAP^{VEGFAKO}$ mice were digested as described in the Method details session and sorted as CD45-/CD31-/Sca1+/PDGFRa+. FAP were purified from male and female mice equally mixed in our experiments.

FAPs were seeded at a density of 10000 cell/cm2 in high–glucose Dulbecco's modified eagle medium (DMEM) (Invitrogen) supplemented with 10% FBS, 1M Sodium Pyruvate, and 2.5 ng/mL bFGF (Invitrogen). Once FAPs reached 80% confluency, adipogenic differentiation was induced with MesenCult™ adipogenic differentiation media (STEM CELL) until day 5. Half of the media was changed every two days.

METHOD DETAILS

Skeletal muscle injury models

Between 10 and 11 week of age, mice received an intramuscular injection of notexin (0.15 μg/TA, Latoxan) or underwent femoral ligation surgery. In femoral ligation, a skin incision was made over the femoral artery beginning at the inguinal ligament and continued caudally to the popliteal bifurcation. The ligation site on femoral artery was identified and the femoral vein and nerve along with connecting tissue were separated away from the artery of the ligation point with tip forceps. Once the ligation site was clear of vein and nerve, an 8–0 silk suture was used to ligate around the femoral artery between epigastric artery and popliteal branch. The skin incision was closed with simple interrupted pattern with 6–0 Vicarly suture.[56] The animals were placed in a clean cage with heating support to recover from anesthesia. Once fully recovered, the animals were returned to its original cage with easily accessible food and hydrogel on the cage bottom. Hindlimbs were collected 3–28 days after damage according to the experiment.

Tissue digestion and cell purification after notexin damage

Mice were sacrificed and their hindlimbs were cut into 2 mm pieces. A single cell suspension was made by a 30-min incubation at 37°C in Collagenase type II solution (Sigma Aldrich; 2.5 U/mL) activated by 10 mM $CaCl_2$ followed by centrifugation at 360 G (5 min at 4°C). The cells were then incubated in a mixture of Collagenase D (Roche Biochemicals; 1.5 U/mL) and Dispase II (Roche Bio chemicals; 2.4 U/mL) and agitated every 15 min. Reaction was stopped by subsequent addition of FACS buffer (PBD, 2mM EDTA, 2% FBS) followed by centrifugation at 1700 rpm (4°C for 5 min). Red cells were lysed by Ammonium-Chloride-Potassium (ACK) buffer (Lonza; 1mL) followed by addition of FACS buffer to stop the reaction. Cells were incubated for 25–30 min at 4°C in the primary antibody mixture in FACS buffer ~3×10^7 cells/mL. Muscle mononucleated cells were stained with FITC anti-CD45 or APC anti-CD45 (AbLab; clone I3/2), FITC anti-CD31 or APC anti-CD31 (eBioscience; clone 390), PECy7 anti-Sca1 (eBioscience; clone D7), biotinylated anti-VCAM (AbLab; clone 429 MVCAM.A) followed by streptavadin-PE (Caltag Laboratories #SA1004-4), APC anti-α7integrin (AbLab; clone R2F2) and Hoechst 33342 (Sigma Aldrich #B2261; 2.5 μg/mL). Influx I or II cytometer (BD) sorters were used. From both PDGFRa EGFP WT and CCR2KO, FAP as CD45-/CD31-/EGFP+, inflammatory cells as CD45+/CD31-, myogenic progenitors as CD45-/CD31-/a7+/VCAM+, and endothelial cells as CD45-/CD31+ were sorted. From NG2 dsRed WT, pericytes as CD45-/CD31-/Sca1-/NG2+ were sorted. Whole skeletal muscle and cells were sorted at 0, 1, 2, 3, 4, 5, 6, 7, 10, 14 days after injury with notexin.

RNA extractions from sorted cell populations

Sorted cell populations were rinsed in diethyl pyrocarbonate water (DEPC; Invitrogen) and then, pelleted and resuspended (800G; 10 min; 4°C) twice. They were then resuspended in RNAzol (Sigma Aldrich; #R4533; 1 mL/1 × 10^7 cells) followed by addition of DEPC water (400 μl aqueous/1m RNAzol) and incubated for 15 min at room temperature. Samples were then centrifuged for 15 min (12000 G; 4°C) and supernatant was precipitated using an equal volume of isopropanol and 1 μL of linear acrylamide at −20°C. On the next day, samples were centrifuged (20000 G; 4°C) and the pellet was washed 3 times with 70% ethanol (diluted in DEPC water) and left to airdry. RNA solutions were stored at −80°C in DEPC water and Superase (Applied Biosystem #100021540; 1:20 dilution).

Flash frozen muscles were mixed in RNAzol (1 mL/TA muscle) and homogenized using a sonicator (Omni International). Lysates were agitated followed by addition of DEPC water (400 μL) and incubated for 15 min at room temperature. All samples were centrifuged for 15 min (12000 G; 4°C) and supernatant was precipitated using an equal volume of isopropanol at −20°C and incubated for 10 min at room temperature. Lysates were spun at 8000 G for 10 min at 4°C and washed and pelleted 3 times with 70% ethanol (diluted in DEPC water). Following airdrying, the pellet was resuspended in DEPC water (100 μL/TA) and Superase (1:20 dilution) and stored at −80°C until use.

Perfusion and tissue collection

Mice were anesthetized with 0.5 mg/g tribromoethanol (Avertin) and a horizontal incision was made above the sternum through the skin and the musculoskeletal layer, to expose the chest cavity and the heart. The right atrium was punctured prior to insertion of a 26 1/2-gauge needle (BD) into the left ventricle. Perfusion was performed using a controlled pressure of 120 mmHg for 3 min using freshly prepared 1% PFA for fixation, followed by 4 min of perfusion with PBS. Skin and fascia were removed from lower limb of the mice, and the hindlimb muscles were harvested from each leg. Whole muscles were stored in 0.5% PFA at 4°C overnight and then transferred into 40% sucrose solution in PBS at 4°C for 24 h. Tissues were then embedded into blocks of O.C.T. Compound (Tissue-Tek) using isopentane cooled with liquid nitrogen. All tissues were then stored at −80ºC. For histological analysis, embedded O.C.T blocks were equilibrated at −20°C and cut into 10 μm sections, ensuring distribution of entire tissue on each slide. Slides were then stored at −80°C until use.

For vascular leakage analysis, each mouse was intravenously injected with 5mg of dextran-Texas Red (50 mg/mL) (Invitrogen #D1864) 10 min before tissue harvesting.

Immunofluorescent staining on frozen sections

Previously cut samples, were brought into room temperature. Autofluorescence was quenched using Sodium Borohydride (Sigma Aldrich #213462; 10 mg/mL) for 1 h and followed by blocking in 2% goat or donkey serum and 0.03% Triton X-100 (Sigma Aldrich) in PBS for 1 h. Sections were then incubated in primary antibodies diluted in the previously used blocking buffer for 1 h or overnight. Slides were washed three times with 0.03% Triton X-100 (PBST) followed by a 1-h incubation in Secondary antibody mixtures in PBST. Primary antibodies used were rabbit anti-laminin (Abcam #15575), mouse anti-collagen (Abcam #ab90395), rat and goat anti-CD31 (Biolegend clone 390 and R&D #AF3628, respectively) and rabbit anti-perilipin (Abcam #ab3526). Secondary antibodies included, donkey anti-rabbit 488 (Invitrogen #A21206), donkey anti-goat 488 (Invitrogen #A11055), donkey anti-rabbit 647 (Invitrogen #A31573), donkey anti-goat 647 (Life Technologies #A21447), as well as goat anti-rabbit 488 (Life Technologies #A11034), goat anti-rat 488 (Invitrogen #A11006), goat anti-rabbit 647 (Invitrogen #A21245). Staining of damage/necrotic areas was performed with donkey anti-mouse IgG1 (Life Technologies #1305303) staining in combination with mouse anti mouse collagen 1. Tissue sections were washed with PBS 3 times for 5 min each and transferred to a beaker of PBS for 10 min followed by a 10-min incubation in DAPI (Sigma Aldrich; 1:1000). Cover slips were mounted on slides using Fluoromount-G (Southern Biotech) and stored at 4°C.

Cytospinned cells and staining

Each mouse was treated with 250 μg Brefeldin A (Invitrogen) in 150 μl of high glucose DMEM. At 12 h after the treatment, mice were sacrificed, muscle tissue collected and digested as previously indicated. Different cell types were purified based on the sorting strategy applied for generating bulk sequencing data, and cytospinned on slides. Staining for VEGFA was performed according to the immunofluorescence protocol above described, using primary antibody rabbit anti-VEGFA (Abcam #ab52917).

Myogenic cell immunofluorescence and TUNEL staining on frozen sections

Frozen mouse TA sections were washed briefly with PBS, fixed with 4% PFA in PBS, followed by quenching and permeabilization with 100mM glycine and 0.5% Triton X-100 in TBS. The buffer with 4% goat serum, 2% BSA, 4% MOM blocking reagent (Vector Labs #MKB22131), 0.1% Tween 20 in TBS, was used for blocking the TA section. The same solution without the MOM reagent was used for primary and secondary antibody staining. Rabbit anti-MyoD (Abcam #ab133627), mouse anti-Pax7 (AbLab #1/10), and rabbit anti-laminin (Abcam #ab11575) antibodies were used for immunofluorescence staining overnight at 4°C, along with goat anti-rabbit IgG conjugated with either Alexa 488 (Thermo Fisher #A11034) or Alexa 647 (Thermo Fisher #A21245) and goat anti-mouse IgG1 Alexa 488 (Thermo Fisher #A21121) as secondary antibodies as the following step for 1h at room temperature the following day. Prior to mounting, nuclei on all sections were counterstained with 600nM DAPI in TBS for 5 min at room temperature.

Apoptotic myogenic cell assays were performed with a TUNEL staining kit (ABP Biosciences A052). TdT catalyzed ligation of biotin-conjugated dUTP was performed at 37°C for 90min as an additional step between permeabilization and blocking, with additional TBS wash steps before and after the reaction. Streptavidin-conjugated AndyFluor647 was added at the same time as secondary antibodies for immunofluorescence. Each time the experiment was conducted, one section was allocated for negative control staining where no TdT enzyme was added, but streptavidin-conjugated AndyFluor647 was still added at the later step. All fluorescence images were acquired with the Nikon Eclipse and Zeiss LSM900 microscopes, quantification was performed in Fiji software.

H&E staining

Muscles were harvested, sequentially fixed in 1% paraformaldehyde (PFA) and incubated in 70% ethanol. Muscles were embedded in paraffin and then sectioned at a thickness of 4 μm using a Leica microtome (RM 2255). Sections were stained with Hematoxylin and Eosin (H&E) (Waxit).

Image acquisition

Tissue sections were visualized on a Y-IFP fluorescent microscope (Nikon Instruments) and a C1 laser-scanning confocal microscope (Nikon Instruments; Eclipse Ti) equipped with lasers at 405, 488, 568, and 633 nm. NIS Elements software was used on

both microscopes for multichannel image acquisition procedure. Single immunofluorescent images were captured using an auto-exposure feature and a hardware gain of 1. Large stitched images were acquired by a 10% overlap and manual refocusing in every 3 frames using the NIS Ar Elements Software (Nikon Instruments). Automatic post processing and shading correction was used to enhance the stitched images. In histology images white balance was set automatically using a white light background. High resolution images were taken using the confocal imaging (Zeiss; Axio Observer).

Histological quantification

Images chosen for analysis were selected based on representativeness in the whole data as well as quality of the tissue section. All quantifications were performed with the NIS Ar Elements software using 3 or more biological replicates for the respective experimental and control groups. Fiber size quantification was performed in notexin-damaged skeletal muscles, where regenerating fibers were identified by presence of center-located nuclei and infiltrating interstitial cells in the fiber, on a laminin stained section. All fibers in 10 images (20X; 300 μm^2) were quantified per animal. Vascular density quantification was performed on both damage models, where CD31 positive structures were quantified on an immunofluorescent-labeled slide. In notexin-damaged muscles, the number of vascular structures was divided by the total section area and 10 images (20X) were quantified from each animal. To characterize the phenotype of mice with femoral ligation, two whole-section stitched images/mouse were quantified. Here, due to vascular irregularities, the percentage of area positive for CD31 was calculated rather than using number of CD31+ vessels per area as applied for notexin injury model. Similarly, to quantify adipose tissue and necrotic areas in skeletal muscle collected from mice with femoral ligation, we calculated the percentage of area positive for perilipin and IgG staining, respectively. Last, the percentage of decellularized area was quantified based on low nuclei numbers (by DAPI staining). All quantifications were carried out using an automatic system where positive structures were masked by an intensity threshold.

Multiplexed immunofluorescence co-detection (CODEX)

Antibody conjugation, validation, tissue staining, image processing and data analysis were performed following Palla et al., 2020.[57]

Perilipin staining

After FAP-adipogenic differentiation, media was removed, cells were quickly rinsed with 1X PBS before being fixed with 4% pFA for 7 min at room temperature. After 2 more washes, blocking buffer (1X PBS 0.3% Triton X-100, 3% goat serum) was applied for an hour at room temperature and primary antibody (Perilipin Abcam #ab3526) was incubated overnight at 4°C. Goat anti-rabbit IgG(H + L) Alexa 488 (Invitrogen #A11034) was used as a secondary antibody. DAPI was used to counterstain the cells. Plates were kept at 4°C until imaging Cells were imaged using an ECHO Revolve microscope.

VEGFA ELISA experiment

Snap frozen muscles from wild type or knockout mice were collected at steady state or after injury. Tissue were homogenized (25 Hz; 30 min; Qiagen 85300) in 500 µl PBS in proteinase inhibitor (1x). Protein quantification was performed using BCA assay kit (Thermo Fisher #23225). The ELISA assay was performed according to the instructions on the ELISA kit (R&D systems; MMV00) using 150 µg of protein for each sample.

Fluorescent activated cell sorting (FACS) analysis

In vivo proliferation assays were performed by intraperitoneal injection of 0.5 mg (10 µg/mg) of Ethidium Bromide (EdU; Thermo Fisher #C10337) 12 and 24 h before sacrificing the animals. Samples were digested as previously indicated. Surface and EdU staining was performed according to the manufacturer's instructions. In vascular perfusion analysis, mice were treated with 50 µL of lectin-fluorescein isothiocyanate (Sigma Aldrich #L0401) diluted with 50 µL of PBS. Mice were sacrificed after 10 min and tissues were collected, digested, and stained as previously indicated.

RNASeq bioinformatics analyses

Bulk-RNA sequencing

RNA quality control was performed with Agilent (Santa Clara, CA, USA) 2100 Bioanalyzer. Qualifying samples (n = 2–6) were then prepped following the standard protocol for the TruSeq stranded mRNA library kit (Illumina, San Diego, CA, USA) on the Illumina Neoprep automated nanofluidic library prep instrument or NEBnext Ultra ii Stranded mRNA (New England Biolabs, Ipswich, MA, USA). Sequencing was performed on the Illumina NextSeq 500 with Paired End 42bp × 42bp reads. Demultiplexed read sequences were then aligned to the Mus Musculus (PAR-masked)/mm10 reference sequence using TopHat splice junction mapper with STAR aligner (https://www.ncbi.nlm. nih.gov/pubmed/23104886).

Filtering and normalization step

In our analysis, we discarded genes that did not have more than 100 raw counts in at least one time point. Additionally, we kept only genes with an expression average of 3 RPKM. With the remaining genes, we performed RUV normalization using RUVSeq R Package (version 1.14.0) to remove unwanted variation from our datasets.[58] We used RUVg function with 3000 invariant genes and Table S3 summarizes the parameters applied in the RUV analysis for each dataset.

PCA and cluster analysis

PCA plots were made using plot PCA function from EDAseq R package [10.1186/1471-2105-12–480]. Using kmeans (stats R package) we clustered the samples in the PC score space. We empirically chose the optimal number of cluster k, with k = {2, …, 10}, using two indexes: silhouette index as implemented in NbClust function from NbClust R package[59] and the biological homogeneity index (BHI) as implemented in BHI function from clValid R package.[60] The BHI was computed using the time/day. In brief, the higher the BHI the most homogeneous are the days within the cluster. When silhouette and BHI showed similar results, we preferred the lower number of clusters.

Differential expression analysis

- Time-wise analysis for cell-population and total muscle

Differential expression analysis was performed on all cell populations and in the total tissue. After filtering our datasets, we computed a set of time-invariant genes defined as the 3000 genes with the highest p values. Using RUVSeq coefficients, we performed differential expression analysis using edgeR (version 3.22.3).[61] We considered differentially expressed the genes with an adjusted p value $\leq$ 0.01 and an absolute log2 Fold Change $\geq$ 2 in at least one comparison of the time points.

- Cell-wise comparison

Differential expression analysis was performed among cells. After filtering our datasets, we computed a set of genes defined as 3000 genes with the highest p value in the cell-wise comparison. Using RUVSeq coefficients, we performed differential expression analysis using edgeR. We considered as differentially expressed the genes with an adjusted p value $\leq$ 0.01 and an absolute log2 Fold Change $\geq$ 2 in any comparison among cell populations.

Time-wise clustering

Differentially expressed genes (DEG) from each cell population and whole tissue were clustered using TCseq R package (version 1.4.0) (http://bioconductor.org/packages/release/bioc/html/TCseq.html). We decided to organize DEGs into 9 clusters given the presence of 10 time points for nearly all cell populations sorted and whole tissue.

Identification of the "active" genes

Based on the centroids of the cluster, we identified the time point were the cluster is activated using binarizeTimeSeries function from BoolNet R package (version 2.1.4).[62] This method is based on kmeans and computes a cutoff according to the centroid values, thereby marking with active = 1 those time points above the cutoff and active = 0 otherwise. All the genes of the cluster inherited the activation pattern of the cluster centroid, therefore we defined a gene active in the population at day d (pop-active$_d$) if it belongs to one cluster "active" at d. We applied this for all cell population and the whole tissue. The pop-active genes in the whole tissue are used for the following point 1) and for the GO enrichment (see Gene Ontology Biological Process enrichment analysis). Along with pop-active$_d$, we created a list of genes called "subset-specific" that potentially reflect cell subset expansion. These genes are 1) DEGs in the whole tissue time wise comparison, and 2) significantly more expressed in one cell type than other two cell types (adjusted p value<= 0.01 and an absolute log2 Fold Change $\geq$ 2). Like pop-active genes, subset-specific genes inherit the temporal activation pattern of the centroid of the cluster they belong in the whole tissue. Genes that were significantly more expressed in one cell type than other two cell types but not DEG in whole muscle, were defined as "constitutively-active" genes and assumed to be always active (active at all time points) because their functions are always required by the cell population.

Ligand-receptor network analysis

The Ligand-Receptor Network (LRN) was built starting from a manually curated ligand receptor interaction dataset from Rezza et al.[1] As described for all genes, we defined the ligands/receptors that are "active" along the time: pop-active$_d$ are the ligands/receptors active at day d in the cell batch, subset-specific$_d$ are the ligands/receptors that are mainly expressed by a cell type where they are either DEGs in the whole tissue or constitutively-active. At any day d, and for each cell type cell, we defined the autocrine cell network at day d (cell-AN$_d$) as the induced subnetwork obtained from the LRN and active ligands/receptors (pop-active$_{d_cell}$ + subset-specific$_{d_cell}$ + constitutively-active$_{cell}$ ligands and receptors). Paracrine cell networks (cell-PN$_d$) were defined as the induced subnetwork obtained from LRN, ligands "active" at day d from all the cell and receptors active at day d in the cell (ligands: pop-active$_d$ + subset-specific$_d$ + constitutively-active; receptors: pop-active$_{d_cell}$ + subset-specific$_{d_cell}$ + constitutively-active$_{cell}$).

Gene Ontology Biological Process enrichment analysis

To understand the function of the genes active at a given day, we performed a day by day GO enrichment analysis. The enrichment was performed on 'pop-active' genes at any day. We limited the analysis to GO Biological Process (GO BP) categories with 10–500 gene members (GO definition from org.Mm.eg.db version 3.8.2).

- GO BP on whole muscle

Enrichment was made for each time point using the 'pop-active' genes in the whole tissue, i.e. those genes that belong to a cluster that is marked as active at a given day in the whole muscle. For this purpose, we used compareCluster from clusterProfiler R package,[63] which allows to directly compare multiple list of genes. We compared the lists of 'pop-active' genes at any time point. Among significant GO BP (any GO at any time point with qvalueCutoff = 0.05) we manually selected the GO BP relevant for this study. We

retrieved 582 significant BP of interest (Table S1). Given the terms redundancies in GO, we manually grouped the relevant GO BP in meta-category by their term similarity. For each group of related terms, we asked the GO BP term with the lowest corrected p value to represent the meta-category. For the dot-plots (Figures 1E–1G and S2A-S2B), we selected 8 relevant meta-category and used dotPlot function (clusterProfiler).

- GO BP in cell population

For each cell population, GO BP enrichment was made for each time point using the pop-active genes. Using compareCluster function we compared the lists of all days simultaneously. Results has been filtered using the BP of interest emerged from whole tissue. Along with the list of interesting BPs, we borrowed from whole muscle analysis also the grouping of the terms in meta-category. As for whole muscle analysis, we asked the GO BP term with the lowest corrected p value to represent the group. Plot were produced using dotPlot function (clusterProfiler).

Trend lines plot for the meta category for the different cell population (as well as WT vs CCR2KO profiles) were created using the average expression of the genes with loadings different from 0 in the PC1. PCS were computed using the Sparse PCA implementation from TimeClip R package (version 0.3.0) on the expression matrix of normalized counts obtained by averaging time replicates.

Gene Ontology biological process on ligand receptors

To better understand the processes driven by the ligand-receptors putative interactions, for each cell, we mapped GO BP on autocrine and paracrine networks. As previously described in whole muscle and cell population analysis, we filtered the results using the total muscle list of interesting BPs.

Protein activity inference

To infer protein activity of the receptors, we applied Viper (Viper R package) analysis to our data. Viper assumes that the expression of transcriptional targets of a protein (i.e. its regulon) can be a reporter of the protein activity itself.

Following an approach previously described,[44] we created the regulatory networks from the cell population dataset (both WT and CCR2KO) and the total wild type tissue. Both datasets were normalized separately as describe earlier (see Filtering and Normalization Step).

We set up a candidate regulator list. A regulator that share two categories was assigned following this priority: ligands, receptors,[1] transcription factors (TF; GO:0003700, GO:0004677, GO:0030528, GO:0004677), transcriptional cofactors (COF; GO:0003712), and signaling pathway related genes (SP: GO:0007165, GO:0005622, GO:0005886).

To create the regulatory networks from the regulator list, we run ARACNE with 100 bootstrap and mutual information (MI) p values threshold 10–8. Cell and total tissue regulatory networks were merged and regulators with a regulon size smaller than 25 co-expressed genes were excluded from the analysis. Viper function were used to create the protein activity matrix of the regulators and the cell population dataset.

TimeClip analysis of protein activity matrix

Time clip analysis (TimeClip R package) was performed using the protein activity matrix. For each cell, day replicates were averaged.[35] TimeClip was performed on the subset of Reactome pathways (from Graphite R package[63,64]) that contain the gene *Kdr*.

Mitotic Index

Mitotic Index was computed based on the work of Dmitrijeva and colleagues[33] as the average mRNA expression of 9 genes previously described[65] (mouse orthologs were manually annotated). Days were grouped into broader categories as following: ‘‘steady’’ for day 0; ‘‘early’’ from 1 to 3 days after NTX; ‘‘middle’’ from 4 to 7 days after NTX; and ‘‘late’’ from 10 to 14 days after NTX.

QUANTIFICATION AND STATISTICAL ANALYSIS

All data is represented as mean ± standard error of the mean (SEM) and the sample number is indicated in the figure legends, where n indicates the number of animals used per group. Data in all figures were obtained from at least 3 independent experiments involving different mice. The significance of differences was assessed with the GraphPad Prism 6 software (GraphPad Software). The normal distribution of all datasets was tested and, depending on the results, multiple comparisons were performed with the parametric one- or two-way analysis of variance (ANOVA) or with the nonparametric Kruskal-Wallis test, while single comparisons were analyzed with the nonparametric Mann-Whitney test or the parametric one-tailed t test. Results with p values of less than 0.05 were considered statistically significant.